Manuscript published in ACS Catal. 2021, 11, 8701−8715 https://doi.org/10.1021/acscatal.1c01900

Unraveling the intermediate reaction complexes and critical role of support-derived oxygen atoms during CO oxidation on single atom Pt/CeO_2

Yubing Lu,[1,%] Shulan Zhou,[2,3,%] Chun-Te Kuo,[1] Deepak Kunwar,[4] Adam S. Hoffman,[5] Alexey Boubnov,[5] Sen Lin,[2,6] Abhaya K. Datye,[4] Hua Guo,[2] Ayman M. Karim[1*]*

1. Department of Chemical Engineering, Virginia Polytechnic Institute and State University, Blacksburg, Virginia 24060, USA

2. Department of Chemistry and Chemical Biology, University of New Mexico, Albuquerque, New Mexico 87131, USA

3. School of Chemistry and Chemical Engineering, Shandong University of Technology, Zibo, 255049, China

4. Center for Microengineered Materials, Department of Chemical and Biological Engineering, University of New Mexico, Albuquerque, New Mexico 87131, USA

5. Stanford Synchrotron Radiation Light Source, SLAC National Accelerator Laboratory, Menlo Park, California 94025, USA

Manuscript published in ACS Catal. 2021, 11, 8701−8715 https://doi.org/10.1021/acscatal.1c01900

6. State Key Laboratory of Photocatalysis on Energy and Environment, College of Chemistry, Fuzhou University, Fuzhou 350002, China

KEYWORDS: Single-atom catalysts, reaction mechanism, CO oxidation

ABSTRACT: CeO_2 supported Pt single-atom catalysts have been extensively studied due to their relevance in automobile emission control and for the fundamental understanding of CeO_2-based catalysts. Though CeO_2 supported Pt nanoparticles are often more active than their single atom counterparts, CeO_2 supported Pt nanoparticles could easily redisperse to Pt single atom under oxidizing diesel conditions. Therefore, to maximize the reactivity of every Pt atom, it is important to fully understand the reaction mechanism of CeO_2 supported Pt single atoms. It is recognized that the reaction mechanism generally involve more than the single atom, with neighboring atoms playing a critical role. Here we report a CO oxidation study on a Pt/CeO_2 single atom catalyst where we can account for all of the neighbors, using in-situ and operando spectroscopies (EXAFS, XANES and DRIFTS). Microcalorimetric measurements provide heats of adsorption and kinetic measurements yield orders of reaction and activation energy. Coupled with computational modeling via density functional theory, we present a comprehensive picture of the dynamics of the surface species, the role of surface intermediates and explain the observed reaction kinetics. We started with a catalyst containing exclusively single atoms and used in-situ/operando spectroscopy to provide evidence for their stability during reaction and to identify the Pt_1 complexes before and during reaction and their binding to CO. The results reveal that in the pre-catalyst, Pt is present as $Pt(O)_4$ on the $CeO_2(111)$ step edge sites but during CO oxidation we find that that two Pt_1 complexes co-exist, representing two states of the active site in the reaction cycle. The dominant state/complex remains $Pt(O)_4$ which adsorbs CO very weakly as shown by CO

microcalorimetry. The second, minority state/complex, $Pt(CO)(O)_3$ is generated through reaction of $Pt(O)_4$ with CO, and CO is bound strongly to Pt_1. Labile oxygen adatoms from the CeO_2 surface play a major role in the reaction to regenerate the $Pt(O)_4$ directly from $Pt(O)_3$ or by reaction with the strongly adsorbed CO in $Pt(CO)(O)_3$ to complete the reaction cycle and regenerate the $Pt(O)_4$ complex. We show that the formation of an oxygen vacancy and generating a labile O* are not barrierless which explains the long lifetime of $Pt(CO)(O)_3$ and its detectability despite being a minority complex. The results help to develop a comprehensive view of the dynamic evolution of Pt_1 complexes along the reaction cycle and provide unprecedented mechanistic insights to guide the design of Pt based single-atom catalysts.

INTRODUCTION

Atomically dispersed noble metals on different supports have gained much attention due to their maximized metal utilization and promise for improving catalytic efficiency.[1-4] Additionally, their fundamentally different electronic properties compared with their nanoparticle counterparts,[2, 4-11] hold potential to perform difficult selective chemical transformations,[12-19] even those traditionally limited to homogeneous catalysts.[20, 21] On a fundamental level, supported metal single-sites with uniform atomic scale structure serve as model systems for bridging the materials gap and studying reaction mechanisms by relating theory and experiment. Therefore, tremendous efforts have recently been devoted to the synthesis of uniform, atomically dispersed catalysts with much success.[4, 22-29] However, there is still a substantial lack of detailed knowledge on the structure-activity relationship and detailed mechanistic steps for these novel classes of catalysts.

Due to its importance for many applications, supported Pt single atoms have been investigated extensively.[4, 13, 16, 26, 30-36] A prototype single Pt atom catalyst is Pt_1/CeO_2, which has attracted intensive attention for CO oxidation because of its importance in exhaust emission abatement, especially for its stability and resistance to oxidation at high temperatures unlike Pt nanoparticles which deactivate when

oxidized.[25, 36-38] Several experimental and theoretical studies of Pt_1/CeO_2 have been reported. stable Pt single atoms on CeO_2 support can be prepared via a high-temperature atom-trapping method where Pt atoms diffuse to stable adsorption sites on the CeO_2 support.[25] Up to 3 wt% Pt loading can be stabilized as single atoms through this atom trapping method to form a stable Pt square planar structure on $CeO_2(111)$ step sites.[24] Pt_1/CeO_2 catalysts can also be synthesized using wet impregnation at lower calcination temperatures.[39, 40] Resasco et al.[40] showed that at low loadings, Pt single-atoms tend to bond strongly on step sites of CeO_2 with good thermal stability but the stability decreases with an increase in metal loading. Density functional theory (DFT) calculations showed that while Pt single atoms on $CeO_2(111)$, (110) and (100) are all thermally stable,[41] the activity and stability during CO oxidation is site dependent. Pt on $CeO_2(110)$ was calculated to be the most thermally stable, and the activity is in the order of $Pt/CeO_2(111)/(100)$ > $Pt/CeO_2(110)$. The site-specific activity and stability indicate that the support stability and the characteristics of Pt binding site are important for the reactivity and stability of the Pt_1 species. The Pt/CeO_2 single-atom catalysts are in general not the most active for CO oxidation. Indeed, many Pt/CeO_2 single-atom catalysts prepared with different methods[25, 36] were reported to be much less active than the Pt/CeO_2 nanoparticle catalyst.[36, 42, 43] However, highly active Pt/CeO_2 single-atom catalysts were also reported recently. For example, Pt single atoms at a twisted CeO_2 surfaces are highly active for low temperature CO oxidation[44]. Besides, the Ga-doped Pt_1/CeO_2[45] showed better activity than the traditional Pt_1/CeO_2. It is clear that Pt_1/CeO_2 prepared with different methods performed differently. Hence, in search for a general guiding principle to the design of Pt_1/CeO_2, it is important to understand the origin of its activity, the rate-limiting step, and the reaction mechanism. More importantly, though in many cases Pt nanoparticles are more active than Pt single atoms, multiple studies clearly showed that the Pt nanoparticles on CeO_2 easily re-disperse into less active Pt single atoms under lean mixtures and oxidizing conditions in a practical diesel engine. Indeed, the redispersion

of Pt particles is known to occur after an oxygen treatment at 400 °C[46] or lean diesel exhaust gas condition at ~ 140 °C and above.[43] Since forming single atoms is unavoidable on CeO_2 supported Pt nanoparticle/cluster catalysts, it is highly desirable to understand the catalytic mechanism of Pt single atoms to improve their activity.

Therefore, connecting the intrinsic CO oxidation activity with the local structure of Pt_1 is crucial to fully understand the reaction mechanism and the factors controlling the reactivity of Pt. While the CO oxidation mechanism on Pt nanoparticles supported on CeO_2 is well understood,[42, 46, 47] many questions remain unanswered for the mechanism on Pt single atoms. Moreover, there is disagreement in the literature regarding the spectroscopic observation of CO adsorption on Pt_1/CeO_2. For example, Pt_1/CeO_2 prepared by atom-trapping was reported to adsorb CO strongly during CO oxidation. The vibrational CO band (ν_{CO}) in DRIFTS (~ 2095 cm^{-1}) was stable in He and O_2 at 180 °C.[24, 25] On the other hand, Pt_1/CeO_2 prepared by impregnation methods showed either no CO adsorption at room temperature[40] or a similar CO peak (~2090 cm^{-1})[39] as that reported[24, 25] on the Pt_1/CeO_2 catalyst prepared by atom-trapping. It remains elusive how a very weakly (or strongly) adsorbed CO on Pt_1 gets oxidized and what role does oxygen from the CeO_2 surface play in the reaction mechanism. Previous studies have demonstrated that the surface oxygen plays an important role for low temperature CO oxidation on Pt supported nanoparticles.[46, 48-51] For example, recent work by our group and by Ganzler et al. showed that the Pt-CeO_2 interfacial sites significantly promote the CO oxidation by supplying reactive/labile O* to overcome the CO poisoning of Pt clusters, [42, 48] and this promotion effect can be further enhanced by CO treatments.[46] However, it is still unclear how the surface/labile oxygen is involved in CO oxidation on single Pt atoms on CeO_2. Hence, to fully realize the advantages of Pt single atom catalysts, it is essential to investigate and fundamentally understand the reaction mechanism to help identify design rules.

Specifically, we need to study the local coordination of Pt single atoms and the adsorption behavior of CO on the as-prepared catalyst and under reaction conditions to identify the reaction intermediates and the rate limiting step(s).

In this work, we combined *in-situ/operando* spectroscopy, micro-calorimetry, and reaction kinetics measurements with first principles calculations to study the catalyst structure and CO oxidation reaction mechanism on a uniform and stable Pt_1/CeO_2 catalyst. We show that in the catalyst before reaction (pre-catalyst), Pt_1 is adsorbed on $CeO_2(111)$ step edge sites as a square planar $Pt(O)_4$ complex. However, during CO oxidation, a combination of infrared and X-ray absorption spectroscopies reveals that two Pt_1 complexes co-exist while we can rule out the presence of Pt clusters based on the *operando* experimental evidence. The dominant state/complex remains $Pt(O)_4$ while the second complex is identified as $Pt(CO)(O)_3$ and is generated through reaction of $Pt(O)_4$ with CO. We show that the CO adsorbs weakly on $Pt(O)_4$ while CO is bound very strongly to Pt in $Pt(CO)(O)_3$. Despite this strong Pt–CO bond in $Pt(CO)(O)_3$, our DFT calculations show that the CO can be oxidized with the involvement of labile surface oxygen (O*) species derived from the CeO_2 surface.

RESULTS

Structure of Pt_1/CeO_2 catalyst before CO oxidation (pre-catalyst). The atomically dispersed Pt supported on CeO_2 was prepared by a high-temperature atom-trapping method as previously reported.[24, 52] Figure 1a and b show representative aberration-corrected high-angle annular dark-field scanning transmission electron microscopy (AC-HAADF-STEM) images showing isolated Pt atoms. We note that no clusters were detected before CO oxidation, and their presence as a minority species can be ruled out since any weakly bound Pt not trapped as single atoms will agglomerate into large Pt nanoparticles at the synthesis temperature of 800 °C in air, which can be easily detected by techniques such as X-ray

diffraction and X-ray absorption spectroscopy.[25] To probe the local environment of the Pt species and their oxidation state, X-ray absorption spectroscopy (XAS) was performed at the Pt L_3-edge. Spectra were collected at room temperature on the as synthesized catalyst and after *in-situ* pretreatment in O_2 at 400 ºC followed by flushing and cooling down in He. The X-ray absorption near edge structure (XANES) spectra are shown in Figure 1e along with reference samples, Pt^{4+} in $Na_2Pt(OH)_6$ and Pt^{2+} in $Pt(acac)_2$. The as-synthesized catalyst showed white line intensity slightly lower than the $Na_2Pt(OH)_6$ indicating that the oxidation state of the Pt single atoms is close to Pt^{4+}. After the *in-situ* pretreatment in O_2 at 400 ºC and cooling down in He, the white line intensity of the single atoms is very similar to the $Pt(acac)_2$, indicating that the Pt single atoms are present as Pt^{2+}. The decrease in oxidation state after 400 ºC in O_2 and cooling in He treatment suggests that O_2 molecules were weakly bonded to Pt single atoms during exposure to air and can be removed during high temperature treatment in He. Given the facile removal of this adsorbed O_2 in He, it is unlikely that the Pt in the pre-catalyst is located as Pt^{4+} in substitutional Ce^{4+} sites.

Further details on the local coordination of the Pt single atoms are revealed by modeling the extended X-ray absorption fine structure (EXAFS) spectra of the Pt_1/CeO_2 and Pt standards (Supplementary Figs. 1-5 and the modeling results are summarized in Table 1). We note that no Pt–Pt back-scattering feature was observed or could be modeled in the Pt_1/CeO_2 EXAFS spectra (Figure 1f, Table 1). Consistent with this picture, the wavelet transform[53, 54] EXAFS of the $Pt_1/CeO2$ after calcination (Figure 1g) shows only one intensity maximum between 5-6 $Å^{-1}$ in *k*-space and 1.5 Å in *R*-space, which corresponds to Pt–O scattering while no Pt–Pt scattering could be seen as compared to the wavelet transform EXAFS of Pt foil. The as-synthesized catalyst showed a Pt–O coordination number of 6 similar to the $Na_2Pt(OH)_6$ standard confirming that Pt_1 is present as Pt^{4+} as also shown by XANES (Figure 1e). The Pt–O coordination number after pretreatment in O_2 at 400 ºC followed by flushing and cooling in He was 3.5

which is similar to 4.0 for Pt in $Pt(acac)_2$ confirming the XANES results that Pt is present as Pt^{2+}. In order to provide more details on the local coordination of the Pt single atoms and their bonding with CeO_2, we fit the EXAFS spectra of the pretreated Pt_1/CeO_2 catalyst using a model containing Pt–O (both short and long) and Pt–Ce single scattering paths. The results in Table 2 show that, on average, Pt is surrounded by ~4 oxygen atoms at 2.01 Å, ~4 Ce atoms at 3.13 Å and ~4 oxygen atoms at 3.56 Å. Pt single atoms on CeO_2(111) terraces were reported to adopt a 6-fold coordination with oxygen atoms at 2.12-2.18 Å which is not consistent with our results.[24, 40, 41] On the other hand, it has been reported that Pt single atoms adsorbed on CeO_2(100) or CeO_2(111) step edge sites are coordinated to 4 oxygen atoms in a square planar geometry. Although Pt adopts a square planar geometry on both surfaces, the distance between Pt and Ce is different. Kottwitz et al.[39] reported a Pt–Ce distance of 3.34 Å for Pt single atoms on CeO_2(100), while our results show a much shorter distance of 3.13 Å. Therefore, in our Pt_1/CeO_2, Pt is likely adsorbed on CeO_2(111) step edges rather than on CeO_2(100).

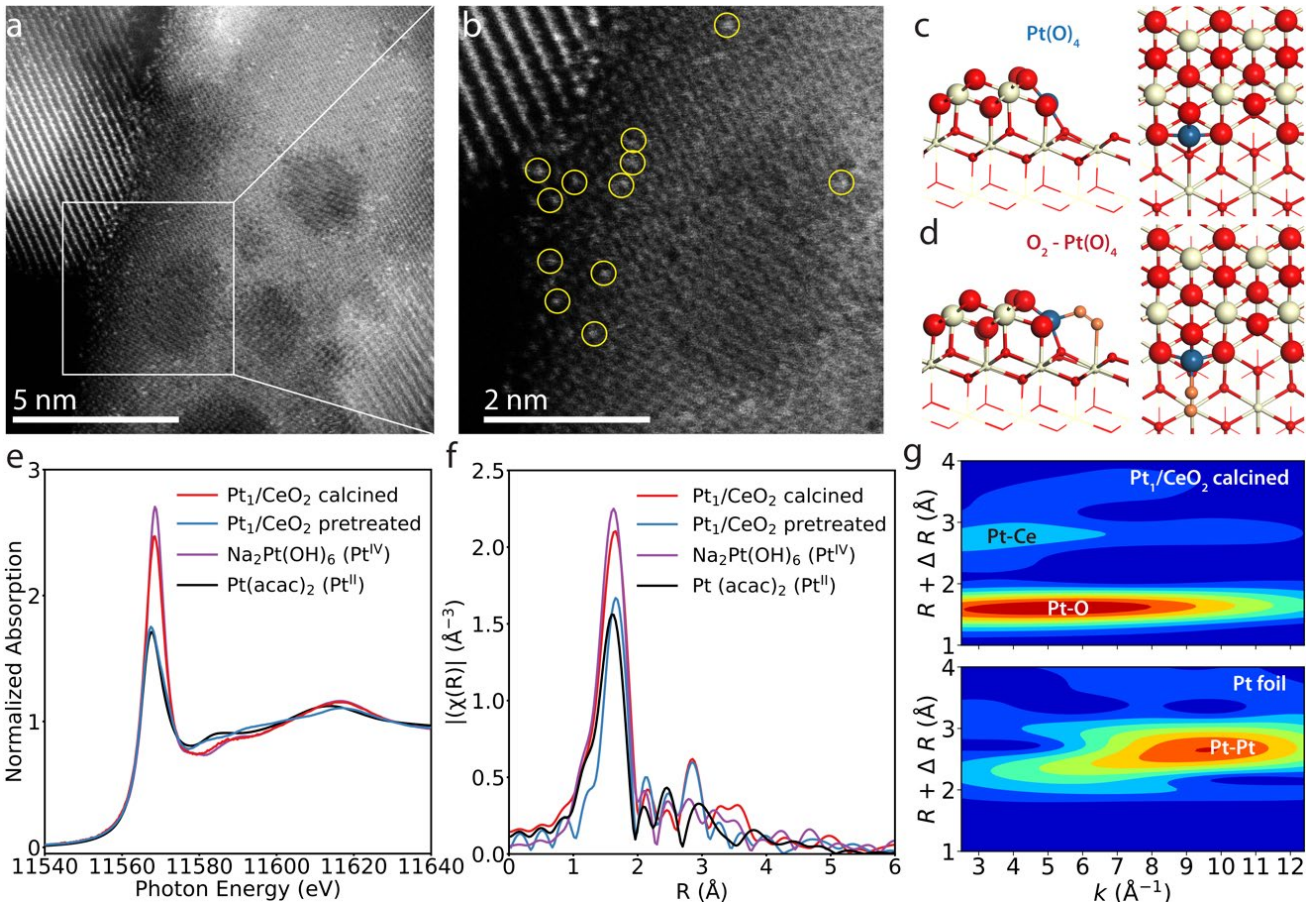

Figure 1. Surface structure of Pt_1/CeO_2 before CO oxidation**. (a)** AC-HAADF-STEM image of 1wt.% Pt_1/CeO_2. **(b)** Enlarged AC-HAADF-STEM image of the region encased by the square in a). **(c)** DFT optimized structure of the Pt single atom on the CeO_2 step edge site with coordination to 4 O. Side and top views. **(d)** DFT optimized structure of weakly adsorbed O_2 on Pt_1/CeO_2 (structure in d). Side and top views. **(e)** Pt L_3 XANES and **(f)** magnitude of the Fourier transformed k^2-weighted $\chi(k)$ data (Δk= 3–12.5 Å^{-1}) in R-space of the 1 wt.% Pt_1/CeO_2 as synthesized (calcined) and after pretreatment. **(g)** wavelet transform for the k^2-weighted $\chi(k)$ signal of the 1 wt.% Pt_1/CeO_2 after pretreatment and Pt foil. Scale bar of wavelet contour: 0-0.064 for Pt_1/CeO_2 calcined; 0-0.08 for Pt foil. $Na_2Pt(OH)_6$ with +4 oxidation state and $Pt(acac)_2$ with +2 oxidation state are shown as standards in **e** and **f**. Color of DFT structures in **c** and **d**: Ce, light yellow; O, red; O_2 physisorbed on Pt, orange; Pt, blue.

Table 1. Summary of EXAFS modeling results at the Pt L_3-edge for the Pt references, 1wt.% Pt_1/CeO_2 catalyst as synthesized (calcined) and, Pt_1/CeO_2 catalyst after pretreatment (O_2 and He treatment at 400 ºC).

	$Na_2Pt(OH)_6$	$Pt(acac)_2$	Pt_1/CeO_2 as synthesized	Pt_1/CeO_2 after pretreatment[a]
$N_{Pt–O}$	6.1 ± 0.7	4.0 ± 0.4	6.1 ± 0.4	3.5 ± 0.4
$R_{Pt–O}$ (Å)	2.00 ± 0.01	1.99 ± 0.01	2.02 ± 0.01	2.02 ± 0.01
$\sigma^2_{Pt–O}$ (Å^2)	0.002 ± 0.001	0.002 ± 0.001	0.002 ± 0.001	0.000 ± 0.001
$\Delta E_{0\ Pt–O}$ (eV)	10 ± 2	9 ± 1	12 ± 1	12 ± 1
Reduced χ^2	487	717	15	67
R-factor	0.003	0.002	0.0007	0.002

[a] Spectrum collected in He at 150 ºC. All the spectra for the other samples were collected in air at room temperature.

Notation: N, coordination number of absorber-backscatterer pair; R, radial absorber-backscatterer distance; σ^2, the mean square displacement of the half-path length and represents the stiffness of the bond for a single scattering path, ΔE0, correction to the threshold energy.

Table 2. Comparison between EXAFS modeling results at the Pt L_3-edge for the Pt_1/CeO_2 catalyst after O_2 and He treatment at 400 ºC and the DFT optimized model of the Pt single atom on CeO_2(111) step edge. The $Pt–O_{long}$ denotes the coordination between Pt and a further away O on CeO_2 surface as shown in the DFT model (Figure 1c).

	EXAFS fit	DFT model[a]
$N_{Pt–O}$	3.4 ± 0.3	4
$N_{Pt–Ce}$	4.1 ± 1.9	4
$N_{Pt–O\_long}$	4.5 ± 1.4	4
$R_{Pt–O}$ (Å)	2.02 ± 0.01	1.9-2.0
$R_{Pt–Ce}$ (Å)	3.13 ± 0.01	3.2-3.3
$R_{Pt–O\_long}$ (Å)	3.58 ± 0.04	3.5-3.6
$\sigma^2_{Pt–O}$ (Å^2)	0.000 ± 0.001	-
$\sigma^2_{Pt–Ce}$ (Å^2)	0.008 ± 0.003	-
$\sigma^2_{Pt–O\_long}$ (Å^2)	0.004[b]	-
ΔE_0 (eV)	12 ± 1	-
Reduced χ^2	53	-
R-factor	0.0032	-

[a] DFT model is shown in Figure 1c.

Notation: N, coordination number of absorber-backscatterer pair; R, radial absorber-backscatterer distance; σ^2, the mean square displacement of the half-path length and represents the stiffness of the bond for a single scattering path, ΔE_0, correction to the threshold energy.

To provide further insights, we performed DFT calculations for Pt single atoms adsorbed on CeO_2(111) step edge sites and the optimized model is shown in Figure 1c. The adsorption energy of Pt at this site of CeO_2 is -705 kJ/mol which is more negative than the cohesive energy of Pt (-534 kJ/mol), underscoring its stability and inclination to exist in the atomic form. The results are consistent with the

well-established ability of CeO_2(111) step edges to trap Pt single atoms and stabilize them against agglomeration at high temperature during the synthesis.[24, 25] Furthermore, the DFT model shows that Pt_1 is surrounded by 4 oxygen atoms with Pt–O distances between 1.89 and 2.03 Å, 4 Ce atoms at 3.2–3.3 Å, 3 oxygen atoms at 3.5 Å and one oxygen atom at 3.61 Å (see Supplementary Figure 6 for the optimized DFT structure and Supplementary Table 1 for the detailed bond distances). The coordination numbers and bond distances are in very good agreement with our EXAFS modeling results. Therefore, we conclude that in the pretreated catalyst Pt_1 is sitting at a CeO_2(111) step edge site and is bound to 4 oxygen atoms, $Pt(O)_4$, in a square planar geometry. This conclusion is also consistent with our previous aberration-corrected STEM results on the same catalyst showing Pt single atoms at step edges of CeO_2(111).[24]

O_2 and CO adsorption on the Pt_1/CeO_2 pre-catalyst. Having established that our DFT model closely matches the experimental results, we investigated the adsorption of O_2 and CO on Pt_1/CeO_2 by DFT calculations and microcalorimetry. The calculated O_2 adsorption energy on Pt_1 in the optimized structure in Figure 1c is -24 kJ/mol (See Figure 1d for the structure with O_2 adsorbed on Pt_1/CeO_2 with square planar $Pt(O)_4$ structure). Calorimetry measurements of O_2 adsorption on Pt_1/CeO_2 showed heats consistent with physisorbed O_2. The initial adsorption energy is around -20–40 kJ/mol (Figure 2a) which is in reasonably good agreement with the DFT calculation results. The results are consistent with the fact that weakly adsorbed O_2 on Pt_1 can be easily removed by treatment in He as observed by EXAFS where the Pt–O coordination decreased from 6 to 4 (Table 1). Additionally, our DFT calculations show that CO adsorption on Pt_1/CeO_2 with square planar $Pt(O)_4$ structure is weak, -42 kJ/mol (see Supplementary Figure 8 for the structure). We measured the CO adsorption energy using microcalorimetry at -75 ºC on the Pt_1/CeO_2 catalyst after *in-situ* treatment in O_2 and He at 400 ºC. As shown in Figure 2a, at low coverage (CO/Pt<0.2), the initial differential heat of CO adsorption was -44

kJ/mol, which is in excellent agreement with the DFT calculation results. This indicates that CO adsorbs weakly on $Pt(O)_4$. State of Pt_1 under reaction conditions. To further characterize the Pt–CO binding and local coordination of Pt_1/CeO_2 under reaction condition, *in-situ*/*operando* DRIFTS and XANES/EXAFS experiments were performed. For both experiments, the Pt_1/CeO_2 was pretreated in O_2 and then He at 400 ºC. After pretreatment, CO oxidation was performed under 3 kPa CO and 2 kPa O_2 for 20 min at 150 ºC and CO_2 was detected in the reactor effluent in the DRIFTS and XAFS experiments (Figure 2b and Supplementary Figure 9). During the *in situ*/*operando* DRIFTS experiment, one major peak at 2096 cm^{-1} was observed in the ν_{CO} region during CO oxidation (Figure 2b) and the peak remained in the same position after flushing the gas phase CO and O_2 with N_2/O_2 (Figure 2c, d). We note that CO peak position (2096 cm^{-1}) and shape were identical on a lower Pt weight loading catalyst (0.2 vs. 1 wt%) showing that the loading does not affect the anchoring site for Pt_1. This is also reflected in their similar kinetics as discussed below. We assign the 2096 cm^{-1} peak to CO adsorbed on Pt single atoms as previously reported.[25, 31, 55] Notably, the adsorbed CO on Pt_1 was stable in N_2 (Figure 2c) and in O_2 (Figure 2d) with no significant change in peak intensity after 5 min in either gas environments at 150 ºC indicating that CO is bound very strongly to Pt_1. Since Pt_1 on $CeO_2(111)$ step edges is present as $Pt(O)_4$ and was shown to adsorb CO very weakly (see above), we hypothesize that the strong CO adsorption is due to reaction of CO with $Pt(O)_4$ to form $Pt(CO)(O)_3$ during CO oxidation, i.e. $Pt(O)_4 + 2\ CO \rightarrow Pt(CO)(O)_3 + CO_2$. In fact, our DFT calculations show that this reaction has a relatively low barrier (62 kJ/mol) and CO is bound strongly to Pt_1 in $Pt(CO)(O)_3$ (see Figure 2f for the structure) with a binding energy of -260 kJ/mol. Furthermore, the stability of this $Pt(CO)(O)_3$ complex indicates that it is an intermediate complex during CO oxidation. We note that we performed *in-situ* CO chemisorption DRIFTS experiment at -75 ºC on Pt_1/CeO_2 before CO oxidation to capture the relatively weak CO adsorption on $Pt(O)_4$. However, the results in Supplementary Figure 10 showed a dominant peak for CO

adsorbed on CeO_2 (2174 and 2156 cm^{-1}), and a very small peak at 2093 cm^{-1} was also detected (20x smaller than the 2096 cm^{-1} peak under reaction conditions). Additionally, a small peak at 2123 cm^{-1} was detected during the flow of CO but was not stable and disappeared once CO was flushed with N_2 indicating a weakly adsorbed CO. The 2123 cm^{-1} peak could be assigned to CO adsorbed on $Pt(O)_4$ similar to a recent report by Maurer et al.[36] (2129 cm^{-1}). The results are consistent with the low CO-$Pt(O)_4$ binding energy calculated by DFT and measured by microcalorimetry and indicate that the majority of Pt atoms are present as $Pt(O)_4$ and adsorb CO weakly. However, the presence of the 2093 cm^{-1} band at -75 ºC along with the slightly higher initial CO (and O_2) heat of adsorption from microcalorimetry (also at -75 ºC) suggest that a minority of Pt sites are already partially reduced (i.e. bound to 3 oxygens instead of 4) and can adsorb CO to saturate their coordination. Therefore, the high 2096 cm^{-1} peak intensity during CO oxidation shows that the initial $Pt(O)_4$ can react with CO to form $Pt(CO)(O)_3$.

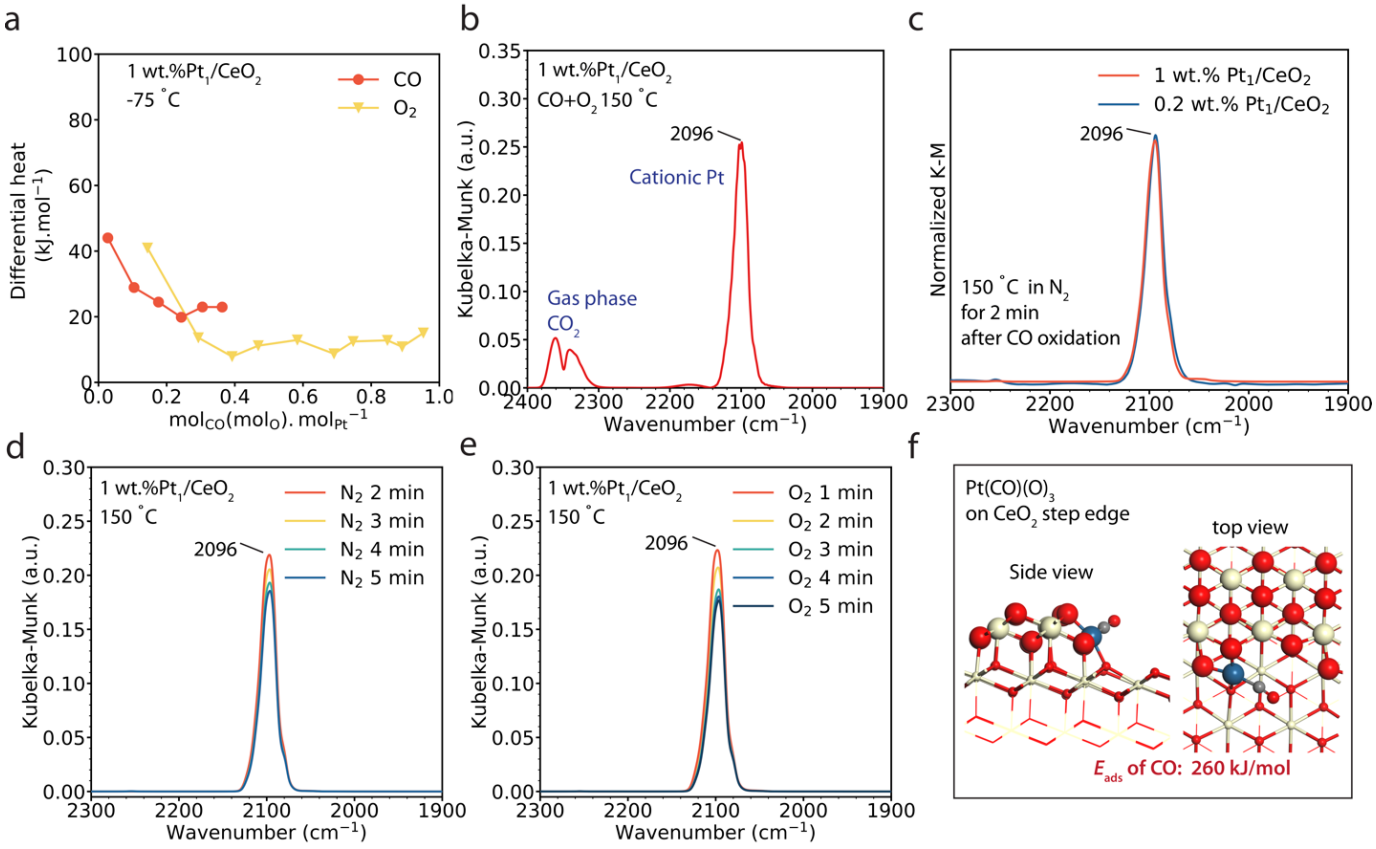

Figure 2. CO/O_2 adsorption and resting state of Pt_1/CeO_2. **(a)** CO/O_2 calorimetry on 1 wt.% Pt_1/CeO_2 after pretreatment in 20 kPa O_2 at 400 ºC for 30 min followed by evacuation under vacuum. The catalyst was cooled to at -75 ºC under high vacuum and CO/O_2 was pulsed onto the catalyst surface. CO/O (1/2 O_2) coverage was normalized to the mol of Pt in the catalyst (nominal loading). **(b)** CO chemisorption DRIFTS of 1 wt.% Pt_1/CeO_2 under CO oxidation at 150 ºC. **(c)** CO chemisorption DRIFTS of 1 wt.% Pt_1/CeO_2 and 0.2 wt.% Pt_1/CeO_2. Spectra were recorded after 20 min CO oxidation at 150 ºC and 2 min N_2 purging to remove the gas phase CO. CO chemisorption DRIFTS characterizing the 1 wt.% Pt_1/CeO_2 catalyst under the N_2 flow **(d)** or O_2 flow **(e)** after CO oxidation. Spectra were recorded after CO oxidation at 150 ºC for 20 min and then short N_2/O_2 (1 kPa O_2) purging to remove the gas phase CO. **(f)** DFT optimized structure of the Pt single atoms on CeO_2 (111) step edge site with 3 O coordination and 1 CO coordination. Condition for b–e: CO oxidation with 3 kPa CO + 2 kPa O_2 and

total flow rate of 50 sccm. Flow rate of N_2 or O_2 step is 80 sccm. Color: Ce, light yellow; O, red; Pt, blue; C, grey.

XANES and EXAFS spectra after the O_2/He pretreatment and during CO oxidation are shown in Figure 3. The XANES spectra (Figure 3a) are almost identical indicating that Pt is maintained as Pt^{2+} under reaction conditions. The EXAFS modeling results (Table 3 and Supplementary Figure 3-4) show a slight decrease in Pt–O coordination from 3.5 in He to 3.2 in CO+O_2 but the difference is within the uncertainty of the fit. A fit that includes adsorbed CO on Pt resulted in Pt–C coordination of ~0.2 at 1.87 Å but the fit was not stable (e.g. after small changes to the range in *k*- or *R*-space or the initial parameter guesses) and therefore is not shown. Wavelet transform plot of the Pt_1/CeO_2 EXAFS during CO oxidation (Figure 3d) showed slightly different magnitude than the pretreated Pt_1/CeO_2 (Figure 3c) at *R*-space ~1.5 Å and *k*-space between 6–12 $Å^{-1}$. The more focused maximum at *R*-space 2.5–3 Å and *k*-space ~4 $Å^{-1}$ could correspond to the contribution of the Pt–CO paths (single and multiple scattering). We note that the differences are small which is consistent with the inability to accurately fit Pt–CO scattering paths in the EXAFS model and indicate that only a small percentage of Pt atoms have CO adsorbed during reaction. In summary, the *operando* XANES and EXAFS results confirm that Pt remains as Pt_1 in Pt^{2+} oxidation state during reaction.

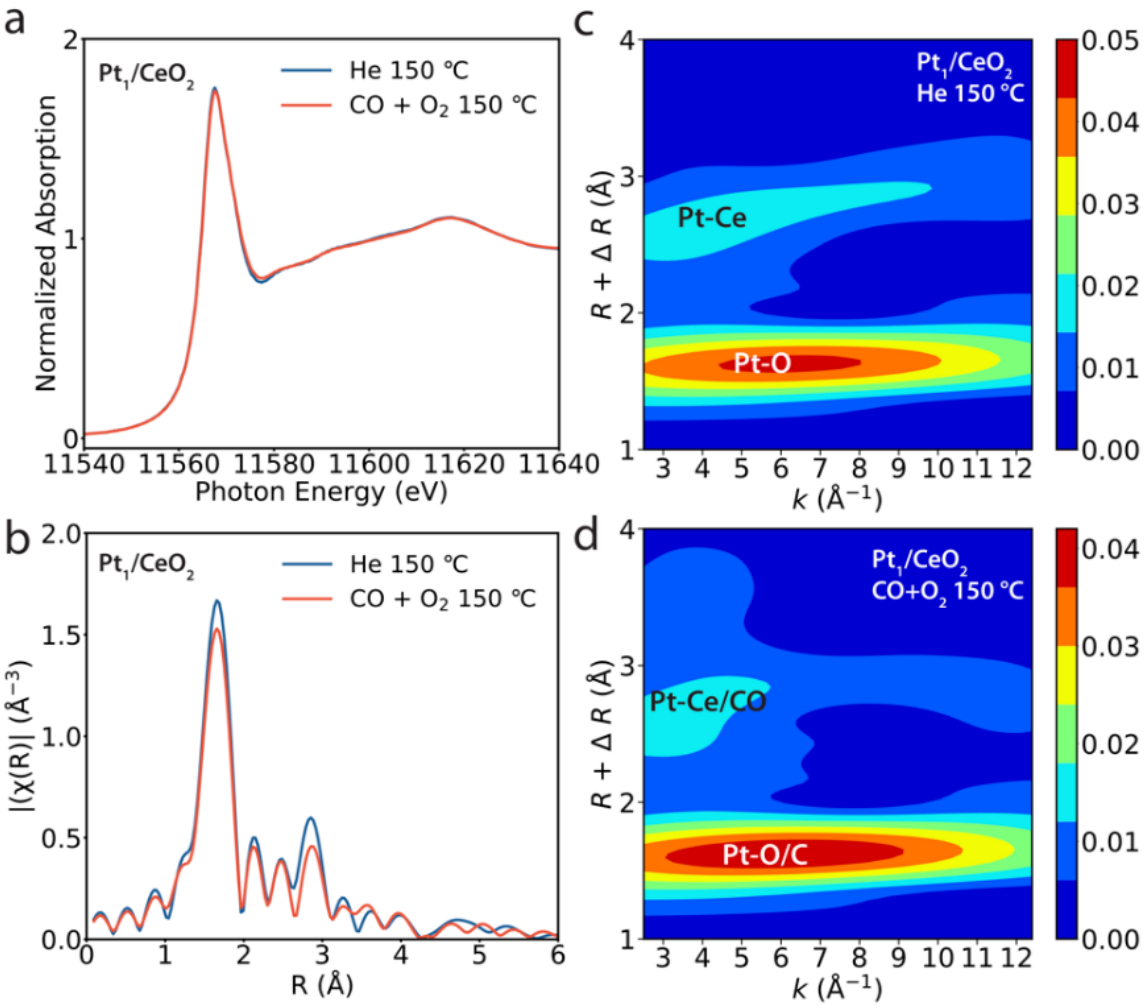

Figure 3. ***Operando*** **XAFS characterization of Pt_1/CeO_2. (a)** Pt L_3 XANES and **(b)** magnitude of the Fourier transformed k^2-weighted $\chi(k)$ data (Δk= 3-12.5 $Å^{-1}$) in R-space of the 1 wt.% Pt_1/CeO_2 catalyst under He flow at 150 ºC and during CO oxidation at 150 ºC, 3 kPa CO + 2 kPa O_2 and total flow rate of 50 sccm. Corresponding wavelet transform of the k^2-weighted $\chi(k)$ signal **(c)** under He flow at 150 ºC and **(d)** during CO oxidation at 150 ºC.

It may appear that *operando* DRIFTS and EXAFS are at odds with what they tell us about the working catalyst, so it is important to note the differences between what they actually measure. Specifically, the DRIFTS experiment is only sensitive to the Pt_1 complexes that are bound to CO, i.e., $Pt(CO)(O)_3$ and not $Pt(O)_4$. On the other hand, EXAFS captures an average of all the Pt in the catalyst.

Therefore, the combined results indicate that the Pt–CO peak detected in DRIFTS represents only a small fraction of Pt which is strongly bound to CO. This is very intriguing and indicates that the DRIFTS spectra only capture one of the Pt single atom intermediate complexes along the reaction pathway. In other words, the EXAFS results show that Pt exists in more than one state under reaction conditions, $Pt(O)_4$ and $Pt(CO)(O)_3$, and only the state bound to CO is detected by DRIFTS (see Supplementary Figure 11 and associated text for further evidence that the majority of Pt_1 is not bound to CO in DRIFTS). Moreover, the EXAFS results suggest that the most abundant state under reaction conditions is $Pt(O)_4$ and not the state detected by DRIFTS, i.e., $Pt(CO)(O)_3$. To our knowledge, the possibility that metal single atoms can be present in more than one stable state during reaction has only previously been reported by computational studies,[56] our work provides the first experimental evidence.

Table 3. Summary of EXAFS modeling results at the Pt L_3-edge for the Pt_1/CeO_2 in He at 150 ºC and during CO oxidation at 150 ºC under 3 kPa CO + 2 kPa O_2.

	Pt_1/CeO_2 in He at 150 ºC	Pt_1/CeO_2 in $CO+O_2$ at 150 ºC
$N_{Pt–O}$	3.5 ± 0.4	3.2 ± 0.3
$R_{Pt–O}$ (Å)	2.02 ± 0.01	2.02 ± 0.01
$\sigma^2_{Pt–O}$ (Å^2)	0.000 ± 0.001	0.000 ± 0.001
$\Delta E_{0\ Pt–O}$ (eV)	12 ± 1	13 ± 1
Reduced χ^2	67	89
R-factor	0.002	0.002

Notation: N, coordination number of absorber-backscatterer pair; R, radial absorber-backscatterer distance; σ^2, the mean square displacement of the half-path length and represents the stiffness of the bond for a single scattering path, ΔE_0, correction to the threshold energy.

CO oxidation kinetics on Pt_1 CO oxidation kinetics on the 1 wt.% Pt_1/CeO_2 catalyst were measured at two different temperatures: 100 and 150 °C (Figure 4). The CO order was 0.7 ± 0.1 and 0.5 ± 0.1 at 100 °C and 150 °C, respectively, and the O_2 order was ~0 at both temperatures. Apparent activation energy (E_{app}) of 69 ± 3 kJ/mol between 80-100 °C was slightly lower than the E_{app} measured between 145–165 °C. To study the effect of loading, which can affect the uniformity of the Pt_1 anchoring sites on CeO_2,[40] the reaction kinetics were also measured on a lower loading 0.2 wt.% Pt_1/CeO_2. Similar positive order in CO (0.8) and a ~0^{th} order in O_2 was also measured on the 0.2 wt.% Pt_1/CeO_2 at 150 °C (Supplementary Figure 13). The E_{app} of 80 ± 1 kJ/mol measured on 0.2 wt.% Pt_1/CeO_2 is also similar to the 1 wt.% Pt_1/CeO_2 (77 ± 1 kJ/mol). The similar kinetics on 0.2 and 1% Pt_1/CeO_2 are not surprising given their identical DRIFTS spectra under reaction conditions (Figure 2c) and confirm the uniformity of the Pt single atoms.

We note that other groups have proposed that transformation of Pt_1 to form metallic clusters may be an essential step to obtain measurable CO oxidation activity below 200 °C.[36] However, our *operando* EXAFS and XANES results (Figure 3a) show that Pt remains isolated (Pt_1) as Pt^{2+} similar to Pt_1 in the pre-catalyst at 150 °C and shows significant CO oxidation reactivity. To further confirm the thermal stability of the Pt_1/CeO_2 during CO oxidation, we also characterized the post-reaction Pt_1/CeO_2 catalyst using *in-situ* DRIFTS at 35 °C (Supplementary Figure 14) as well as AC-HAADF-STEM (Supplementary Figure 15). No metallic Pt or Pt clusters were observed on the post-reaction catalyst which confirmed the excellent thermal stability of Pt_1/CeO_2 during low-temperature CO oxidation. Furthermore, the reaction kinetics (orders and E_{app}) are a signature of the active site and are sensitive to the presence of different types of sites,[11, 56] which in the case of Pt/CeO_2 would be Pt single atoms and Pt clusters. The reaction kinetics on Pt_1/CeO_2 shown in Figure 2 are substantially different from those measured on Pt clusters (see previous work[42] and Supplementary Figs. 11-12 and associated text in the

SI for effect of cluster formation on kinetics) which combined with our *operando* and post-reaction characterizations clearly show that Pt single atoms (Pt_1) are responsible for the measured activity and kinetics.

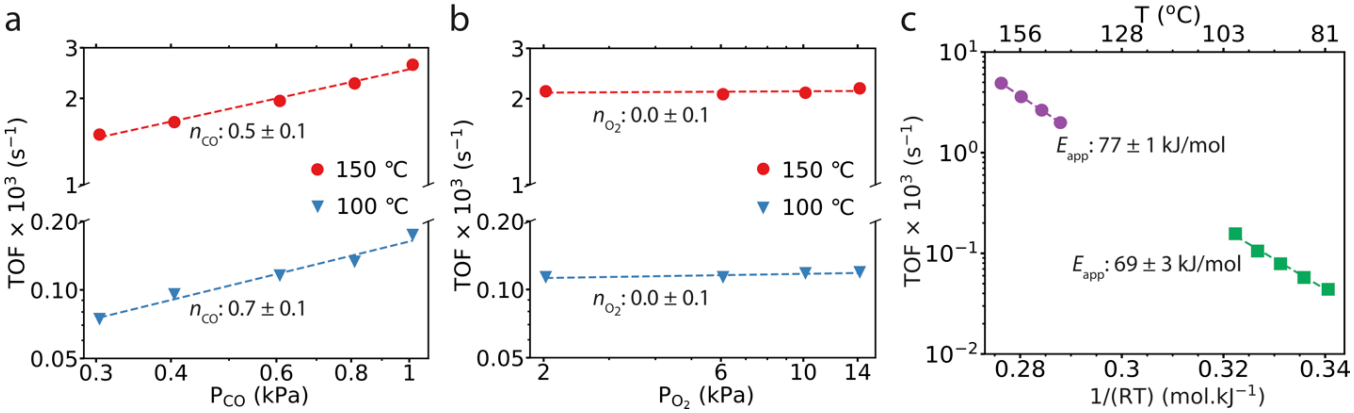

Figure 4. CO oxidation kinetic measurement on 1 wt.% Pt_1/CeO_2. Effect of CO **(a)** and O_2 **(b)** partial pressure on the TOF on 1 wt.% Pt_1/CeO_2 measured at both 150 ºC and 100 ºC. P_{O_2} = 10 kPa, P_{CO} = 0.3–1 kPa in a; P_{CO} = 1 kPa, P_{O_2} = 2–14 kPa in b. **(c)** E_{app} of 1 wt.% Pt_1/CeO_2 measured at two different temperature regions. Region 1: between 145 and 163 ºC. Region 2: 80-100 ºC. Measured with 2 kPa CO and 1.5 kPa O_2 and 50 sccm total flow rate.

We now discuss the mechanistic implications of the reaction orders measured on Pt_1 (Figure 4). Overall, the positive reaction order in CO indicates that the Pt single atoms are not poisoned (kinetically) by CO. Additionally, the ~0th order in O_2 indicates that O_2 activation is facile. The reaction orders suggest that the reaction follows an Eley-Rideal/Mars-van Krevelen mechanism. However, in order to have a positive reaction order in CO, the rate limiting step would likely involve a reaction of CO with an O bound to Pt_1 in one of the resting states, either $Pt(O)_4$ which adsorbs CO weakly or $Pt(CO)(O)_3$ in which CO is adsorbed strongly. Additionally, $Pt(CO)(O)_3$, was not affected by O_2 (Figure 2e) suggesting that an oxygen vacancy needs to be created by CO before O_2 can be adsorbed and activated. Dosing CO on the catalyst at 150 °C (after flushing CO and O_2 with N_2) to simulate the half

reactions involved in an Eley-Rideal/Mars-van Krevelen mechanism lead to overreduction and agglomeration of Pt (Supplementary Figs. 11-12). However, despite the overreduction of Pt in pure CO, the experimental results suggest that CO is needed to create a vacancy site where O_2 gets activated, but it is not clear whether this vacancy is adjacent to one of the Pt_1 complexes or on a nearby site on CeO_2 and which reaction step is rate limiting. To answer these questions about the possible reaction mechanism, we performed DFT calculations starting from Pt_1 on the CeO_2(111) step edge site.

Reaction mechanism from DFT. The proposed reaction pathways calculated by DFT are shown in Figure 5. The reaction cycle starts with $Pt(O)_4$ (i) where four lattice oxygens are bonded with one Pt single atom. In the next step, CO weakly adsorbs to form $Pt(O)_4(CO)$ (ii) and the adsorption energy of CO is -42 kJ/mol. The adsorbed CO facilely reacts with one lattice O to form a bent CO_2 intermediate (iii) (-174 kJ/mol energy change). In the next step the adsorbed CO_2 on Pt (iv) is formed with an endoergicity of 22 kJ/mol. Subsequently, the formed CO_2 desorbs with a 40 kJ/mol barrier, leaving behind the $Pt(O)_3$ (v) structure (Supplementary Figure 16). From $Pt(O)_4$ (i) to $Pt(O)_3$(v), the overall reaction barrier is 62 kJ/mol. The $Pt(O)_3$ (iv) structure leaves an oxygen vacancy next to the Pt. This vacancy can be filled by either CO or O_2. Energetic calculations show that the adsorption energy of CO (v to vi) is -260 kJ/mol, which is much higher than that of O_2 (-96 kJ/mol, v to vi', see Supplementary Figure 17 for detailed structure). Given the strong adsorption of CO, the results suggest that $Pt(CO)(O)_3$ is likely the intermediate complex observed in our *in-situ/operando* DRIFTS experiments. The oxidation of such strongly adsorbed CO (vi) by the co-adsorbed O_2 (vii) to recover $Pt(O)_4$ and release a CO_2 (ix) is difficult with a high barrier of 156 kJ/mol. Interestingly, this $Pt(CO)(O)_3$ intermediate can be rescued by labile oxygens (O*) which are presumably generated via O_2 dissociation at the available oxygen vacancies over ceria (Supplementary Figs. 18–19 and Supplementary Tables 2–3 and associated text for further discussion on the formation of labile O*s). As shown in Figure 5, the DFT results

suggest that the CO adsorbed on $Pt(O)_3$ (vi) could easily combine with a nearby labile O* (vii′) adsorbed on the lower surface of the step to form a bent CO_2 (ix′) with a low barrier of 31 kJ/mol. This step is highly exothermic (-181 kJ/mol). Subsequently, a second labile O* (x′) adsorbed nearby recovers $Pt(O)_4$ (i) at the $CeO_2(111)$ step edge by overcoming a small barrier of 22 kJ/mol, and in the meantime facilitates the desorption of CO_2 (xii′). Alternatively, the $Pt(O)_3$ species (v) can also be converted directly to $Pt(O)_4$ (i) by the same labile O*, which is an exothermic (-342 kJ/mol) process with a minor barrier of 11 kJ/mol. This can be a reason for the low concentration of $Pt(CO)(O)_3$ detected experimentally. We note in passing that no entropic contribution is considered in Figure 5, which could significantly influence the rate constants via the entropic contributions.

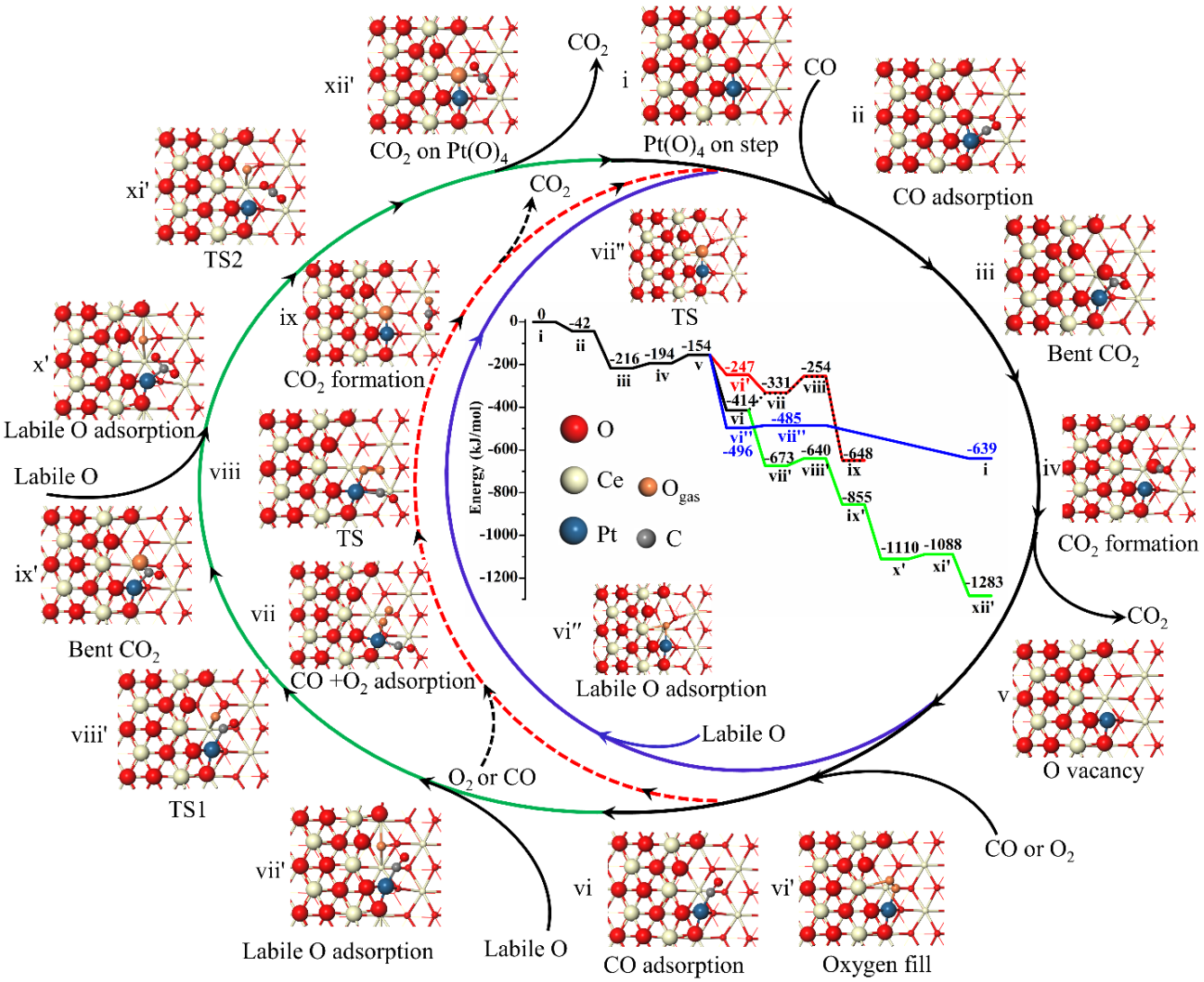

Figure 5. Reaction pathways of CO oxidation on Pt_1 at $CeO_2(111)$ step edge site proposed by DFT calculations. Color: Ce, light yellow; O, red; Pt, blue; C, grey; O in O_2 and labile O, orange. Details on the generation of oxygen vacancies and labile oxygen reaction steps can be found in the supplementary information. The energy is given in kJ/mol.

The existence of labile O* on ceria-based material is well known,[42, 57-59] but its formation and diffusion are not well understood. Although a complete elucidation of these steps, which will require a large-scale kinetic Monte Carlo simulation, is beyond the scope of this work, we show in the SI that the

presence of Pt_1 significantly enhances the formation of O* species on ceria. In CO oxidation, the formation is likely initiated by the reaction between the impinging CO and a lattice oxygen, leading to a gaseous CO_2 and an oxygen vacancy on the surface. While this reaction is exothermic, it is not without a barrier. In fact the barrier is ~72-78 kJ/mol as shown in Supplementary Figure 20 and Supplementary Table 4. This step is probably followed by O_2 adsorption at the vacancy and its dissociation (facile, see Supplementary Table 3), resulting in the labile O* species. However, due to the presence of a reaction barrier (72-78 kJ/mol) for creating the vacancy, the concentration of labile O* will be dependent on CO concentration and temperature and this in turn will affect the dominant reaction pathway and most abundant Pt_1 intermediate complex which is discussed below.

The complete understanding of the kinetics requires more detailed kinetic Monte Carlo simulations, which are beyond the scope of this work. However, the putative reaction pathways in Figure 5 provide important insights on the CO oxidation mechanism on Pt_1/CeO_2. To simplify the reaction pathways and connect theory to experiments, we summarize in Scheme 1 the key reactions and intermediates from the blue and green pathways in Figure 5. As shown in Scheme 1, the CO adsorption on $Pt(O)_4$ is equilibrated, but $Pt(O)_4$ is favored due to the weak CO binding. Consequently, the formation of $Pt(O)_3$ is limited by the low concentration of $Pt(CO)(O)_4$ and the barrier for CO_2 formation/desorption. Once $Pt(O)_3$ is formed, its oxidation to $Pt(O)_4$ can go through two possible pathways (blue or green) depending on temperature and the concentrations of CO and labile O*. Notably, the regeneration of $Pt(O)_4$ from $Pt(O)_3$ through either of the pathways in Scheme 1 involves low reaction barriers. Consequently, the availability/concentration of nearby labile O* dictates which pathway the oxidation of $Pt(O)_3$ will follow (blue or green in Figure 5 and Scheme 1) and the relative amounts of $Pt(CO)(O)_3$ and $Pt(O)_4$. Specifically, if the availability of labile O* is unlimited, the reaction would follow the blue pathway in Figure 5/Scheme 1 where $Pt(O)_4$ is the dominant intermediate Pt_1 complex. Additionally, the

overall reaction rate would be limited by the adsorption of CO on $Pt(O)_4$ and reaction to form $Pt(O)_3$. On the other hand, if the concentration of labile O* is very low, the reaction would follow the green pathway in Figure 5/Scheme 1, the oxidation of $Pt(CO)_3$ will be the rate limiting step and $PtCO)(O)_3$ would become the most abundant Pt_1 intermediate complex.

The above analysis is consistent with our *in-situ/operando* characterization and the measured reaction orders. First, the positive CO reaction order measured experimentally is consistent with the rate limiting step either involving weak CO adsorption/reaction on $Pt(O)_4$ (blue pathway) and/or CO reaction to generate a vacancy on CeO_2 (green pathway). Additionally, the zeroth order in O_2 is consistent with the facile O_2 activation on CeO_2 (Supplementary Table 3). Second, our *in-situ* and *operando* EXAFS and DRIFTS measurements confirm the existence of both $Pt(O)_4$ and $Pt(CO)(O)_3$ complexes. Furthermore, under our experimental conditions (150 °C, 1 kPa CO and 10 kPa O_2) $Pt(O)_4$ is the dominant intermediate Pt_1 complex while $Pt(CO)(O)_3$ is a minority species. The results indicate that [O*] is somewhat limited, resulting in a combination of the blue and green pathways in Figure5/Scheme 1. Moreover, the stability of the $Pt(CO)(O)_3$ peak in O_2 observed in DRIFTS (Figure 2e) further confirms that CO is required to create a vacancy to activate O_2 and create labile O*. In summary, through a combination of detailed *in-situ/operando* characterization, reaction kinetics and DFT calculations we provided a detailed account of how Pt_1 catalyzes CO oxidation and the important role of labile O* from CeO_2 in the reaction cycle. More importantly, the participation of labile O* provided by CeO_2 reconciles the presence of Pt_1 intermediates with strong, and weakly adsrobed CO, namely $Pt(CO)(O)_3$ and $P(O)_4$.

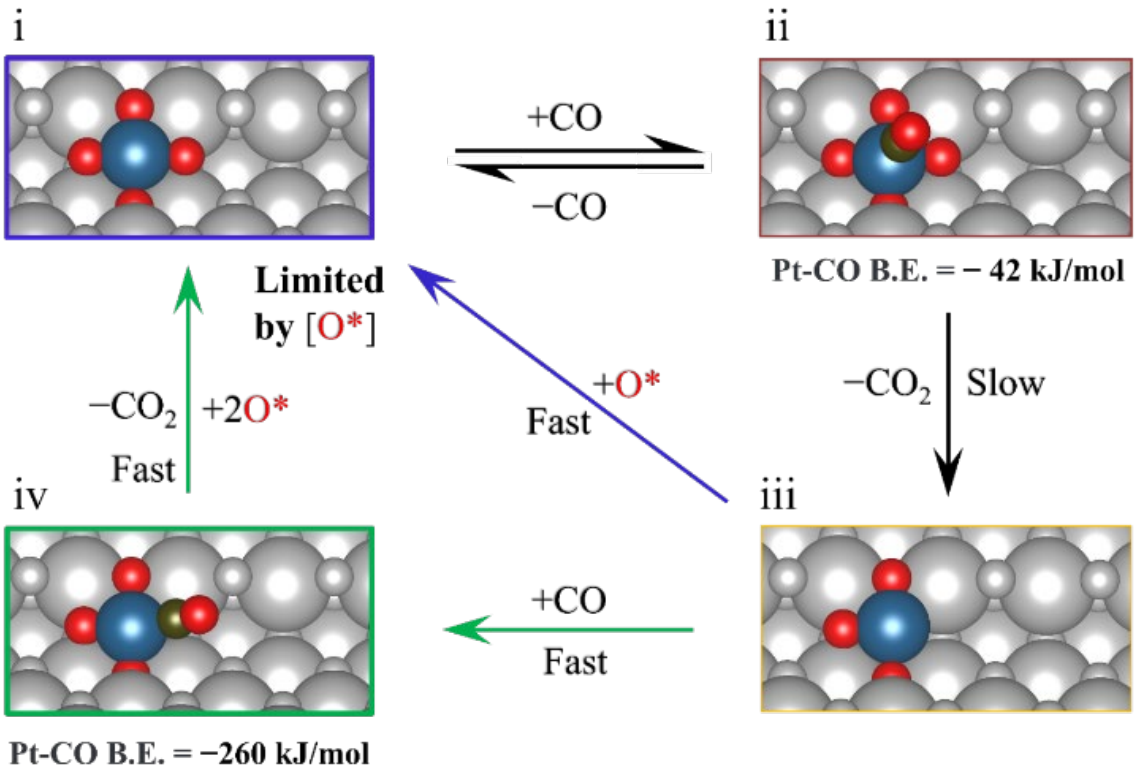

Scheme 1. Key reaction steps and intermediate complexes for CO oxidation on Pt_1/CeO_2. (i) denotes $Pt(O)_4$, (ii) denotes $Pt(CO)(O)_4$, (iii) denotes $Pt(O)_3$ and (iv) denotes $Pt(CO)(O)_3$. O* denotes labile/reactive oxygen provided by CeO_2. The $Pt(O)_4$ (i) and $Pt(CO)(O)_3$ (iv) intermediate complexes were observed experimentally during CO oxidation. The CO adsorption on $Pt(O)_4$ (i to ii) is equilibrated but the $Pt(CO)(O)_4$ complex is not detected experimentally during CO oxidation due its very low concentration (very weak CO binding, -42 kJ/mol). $Pt(CO)(O)_4$ reaction to $Pt(O)_3$ (ii to iii) is slow because of the reaction barrier and low $Pt(CO)(O)_4$ concentration. CO adsorption on $Pt(O)_3$ (iii to iv) is facile with a high CO adsorption energy (-260 kJ/mol). The CO in $Pt(CO)(O)_3$ (iv) reacts with labile O* with relatively low barrier (green pathway). Alternatively, $Pt(O)_3$ can react directly with labile O* to regenerate $Pt(O)_4$ (blue pathway). However, both of these pathways are limited by the generation of labile O* which is initiated by the gas phase CO reaction with CeO_2.

DISCUSSION

Pt single-atom catalysts provide exciting opportunities for understanding the reaction mechanism at the atomic scale and how to tune the local structure of Pt atoms to design more active catalysts. Recent reports show that the reactivity of Pt_1 is strongly dependent on the support. For example, Pt single atoms on small CeO_2 clusters supported on TiO_2 are more active than Pt single atoms on TiO_2 or CeO_2.[60] Additionally, CO oxidation reactivity on Pt_1/TiO_2 was dependent on the local coordination of Pt after different pretreatments.[30] However, the local coordination of Pt single atoms and their binding with CO/O_2, especially under CO oxidation reaction conditions, can be complicated leading to what seems to be contradictory results in the literature. For Pt_1/CeO_2 as an example, Resasco et al. showed that the highly uniform and low-loading Pt_1/CeO_2 single-atom catalyst adsorbs CO very weakly which is difficult to be observed by CO chemisorption in DRIFTS.[40] Our microcalorimetry, EXAFS and DRIFTS results confirm the weak adsorption of CO on Pt_1 due to the saturated coordination of Pt_1 present as $Pt(O)_4$ on $CeO_2(111)$ step edge sites. However, in other studies, CO was reported to be adsorbed strongly on Pt_1/CeO_2 during CO oxidation.[25, 31] For example, multiple studies show a strong CO adsorption peak at 2090-2100 cm^{-1} over Pt_1/CeO_2,[25, 31, 44] but the activities of these reported Pt_1/CeO_2 catalysts are totally different. This cannot be explained by the typical MvK or LH mechanism if $Pt(CO)(O)_3$ is the only active species. Our results suggest this is because $Pt(O)_4$ and $Pt(CO)(O)_3$ co-exist as intermediates in the same reaction cycle. Specifically, we demonstrate that the complex observed in FTIR with a peak located between 2090-2100 cm^{-1} is $Pt(CO)(O)_3$ which is an intermediate along the reaction cycle that starts with $Pt(O)_4$. However, the $Pt(O)_4$ complex cannot be observed in the FTIR due to the weak CO adsorption. Furthermore, despite the strong binding of CO to Pt in $Pt(CO)(O)_3$ (-260

kJ/mol), the reaction with labile O* can regenerate $Pt(O)_4$. Additionally, the relative amounts of $Pt(O)_4$ and $Pt(CO)(O)_3$ depends on the on the reducibility of $Pt(O)_4$ and concentration of labile O* supplied by CeO_2. These results show that despite detecting the same intermediate $Pt(CO)(O)_3$ complex in FTIR on different catalysts, the activity depends strongly on the reducibility of Pt(O)4 and CeO_2 and concentration of labile O*. Our work therefore reconciles the seemingly contradictory results in the literature, especially about the connections between FTIR observed structure and the catalytic performance, and demonstrate that the differences observed are directly related to the presence of more than one resting state (reaction intermediate complex) of Pt_1 during reaction and the difficulty in quantifying the reducibility of CeO_2 and its supply of labile O* .

We should re-emphasize that both Pt_1 complexes detected experimentally are part of the reaction cycle where the $Pt(O)_4$ complex adsorbs CO weakly, and therefore needs to be activated into $Pt(O)_3$ by reaction with CO which appears to be the rate limiting step. Then to regenerate $Pt(O)_4$, depending on temperature, [O*] and [CO], labile O* from the CeO_2 surface can either directly fill the vacancy of $Pt(O)_3$ or reacts with $Pt(CO)(O)_3$. Our results therefore highlight the importance of using more than one *in-situ*/*operando* characterization technique coupled with first-principles calculations for correctly assigning the local structure of the Pt single-atoms. More importantly, by detecting the intermediate Pt single-atom reaction complexes and connecting the reaction kinetics with the reaction energies from DFT calculations, we provide a complete picture of the reaction mechanism and the limiting steps. In particular, our results show the potential for modifying the local environment of Pt_1 to overcome the weak CO adsorption and increase the availability of labile O*. The results will be used to further guide future design of more active Pt single-atom catalysts.

CONCLUSIONS

Manuscript published in ACS Catal. 2021, 11, 8701−8715 https://doi.org/10.1021/acscatal.1c01900

We studied the mechanism of CO oxidation on a single-atom Pt/CeO_2 catalyst and its binding with adsorbates using microcalorimetry, *operando* spectroscopies, kinetic measurements and DFT calculations. We show that in the pre-catalyst Pt single atoms are stabilized as $Pt(O)_4$ on $CeO_2(111)$ step edge sites. The $Pt(O)_4$ is coordinatively saturated and microcalorimetry and DFT calculations reveal that it binds weakly to O_2 and CO, -24 and -42 kJ/mol, respectively. During CO oxidation, *operando* EXAFS and DRIFTS show that Pt remains as single atoms and is present as two intermediate complexes, $Pt(O)_4$ and $Pt(CO)(O)_3$, where the latter binds CO strongly (-260 kJ/mol from DFT calculation). A reaction mechanism was proposed based on our *operando* characterization and reactivity measurements to explain the kinetics and role of intermediate complexes. DFT calculations show that the reaction is limited by the initial reaction between CO and a lattice oxygen coordinated to $Pt(O)_4$ to produce $Pt(O)_3$ which can react with labile O* to regenerate $Pt(O)_4$ or react with CO to form $Pt(CO)(O)_3$. More importantly, our DFT calculation results show that despite the strong CO binding to Pt in $Pt(CO)(O)_3$ (-260 kJ/mol), a labile O* from the CeO_2 surface reacts with CO with a low barrier and completes the reaction cycle. The proposed mechanism is consistent with the reaction orders measured experimentally. The results show the complex dynamic evolution of intermediate single atom complexes along the reaction cycle and provide mechanistic insights to help guide the design of Pt based single-atom catalysts.

EXPERIMENTAL AND COMPUTATIONAL DETAILS

Catalyst preparation and pretreatment. High surface area ceria powder (obtained from Solvay, grade HSA 5) was used as a support. The Pt/CeO_2 catalysts (0.2 and 1 wt.% Pt, nominal) were prepared

by incipient wetness impregnation. The pore volume of ceria (0.6 ml/g) was determined by first wetting the dry ceria powder with water. Impregnation of the platinum precursor was done to fill the pores of ceria. The tetraamine platinum nitrate solution was loaded on ceria and dried at 110 °C for 4 hours until all the water evaporated in air after each impregnation. The sample was then calcined in a tube furnace with 100 ml/min of air for 10 h in air at 800 °C. The furnace temperature was ramped up at 1 °C per minute.

Aberration-corrected high-angle annular dark-field scanning transmission electron microscopy. The catalyst powder was mounted on Cu TEM holey carbon films by simply dipping the TEM grid into the powder. The electron microscope was a JEOL ARM200CF (NEOARM) operated at 200 kV. The microscope is equipped with a spherical aberration corrector (will have to look up the model used). The images were obtained using the high angle annular dark field (HAADF) mode.

Diffuse-reflectance infrared Fourier-transform spectroscopy (DRIFTS). DRIFTS was used to characterize the interaction of the supported Pt catalyst with CO, O_2 and the support. The *in-situ* DRIFTS experiments were performed using a Thermo Scientific IS-50R FT-IR equipped with an MCT/A detector. A spectral resolution of 4 cm^{-1} was used to collect spectra, which are reported in the Kubelka-Munk (KM) units. Approximately 50 mg sample (25–90 μm diameter particles) was loaded in the Harrick Praying Mantis high-temperature DRIFTS reaction chamber. The chamber was sealed and connected to a flow system with temperature control, and gases were flown through the sample at atmospheric pressure. Each reported spectrum is an average of 32 scans. The Pt_1/CeO_2 was pretreated *in-situ* in the DRITS cell before collecting the spectra. The gas pretreatment procedure was the same as mentioned above. For *in-situ* pretreated catalyst, a spectrum under N_2 after the pretreatment was collected as the background.

X-ray absorption spectroscopy (XAS). The catalysts were characterized by *in-situ* XAS at the Pt L_3-edge (11564 eV) using an in-house built cell with a 4 mm ID glassy carbon tube[62]. The XAS measurements were performed at the Stanford Synchrotron Radiation Light Source (SSRL) at beamline 9-3 in fluorescence mode. Beamline 9-3 is a 16-pole, 2-Tesla wiggler side station with vertically collimating mirror for harmonic rejection and a cylindrically bend mirror for focusing. The photon energy was selected using a liquid-nitrogen-cooled, double-crystal Si (220) $\phi = 90°$ monochromator. The catalyst and standard samples were scanned simultaneously in transmission and fluorescence detection modes using ion chambers and a 100-element solid-state Ge monolith detector (Canberra). An Pt standard (Pt foil) was scanned simultaneously with each sample for energy calibration. Step-scanning X-ray absorption spectra were measured from 11334 eV to 12554 eV, corresponding to photoelectron wave number $k = 14.5$ Å^{-1}. The catalyst was pretreated similar to before the catalytic measurements then exposed to CO oxidation conditions. XANES and EXAFS data processing and analysis were performed using Athena and Artemis programs of the Demeter data analysis package[63, 64]. For each catalyst, four scans were collected and merged after alignment. $\chi(k)$ was obtained by subtracting smooth atomic background from the normalized absorption coefficient using the AUTOBK code. The theoretical EXAFS signals for Pt–O, Pt–Ce and Pt–O_{long} for Pt_1 adsorbed on CeO_2 were generated using the FEFF6 code[65] from a manually constructed Pt atom adsorbed on CeO_2. Additionally, the theoretical EXAFS spectra were also calculated using the optimized DFT model reported in Figure 1 and the fit results were almost identical. The theoretical EXAFS signals were fitted to the data in R-space using Artemis by varying the coordination numbers of the single scattering paths, the effective scattering lengths, the bond length disorder and the correction to the threshold energy, ΔE_0 (common for all paths since they are all from the same FEFF calculation). S_0^2 (the passive electron reduction factor) was obtained by first analyzing the spectrum for the Pt foil, and the best fit value (0.84) was fixed in the fit. The k-range used

for fitting was 3-13 $Å^{-1}$ while the R-range was 1.2-3.4 Å for the model that only includes the Pt-O scattering shell and 1.2-3.4 Å for the extended model that also includes the Pt-Ce and Pt-O_{long} scattering paths. The best parameters fit using k-weights of 1,2,3 (simultaneously) in Artemis are reported, however, the results were very similar to those using only a k-weight of 2. Additionally, small differences in the k-range did not have a significant effect on the best fit values of the model fit but did affect their uncertainties. The wavelet transform provides information for both the radical distance and in *k*-space. The continuous Cauchy wavelet transform[66] (CCWT) was used to decompose the EXAFS amplitude terms in R- and k-space giving insight into scatter path contributions and subtle variations in the paths that may not be apparent looking at only the k- or R-space. CCWT was implemented through the Larch package[67]. The k^2-weighted CCWT used a k-range of 0-12.5 $Å^{-1}$ and a R-range of 0.2-6 Å with N_{fft} set to 2048.

Micro-calorimetry. Micro-calorimetry was performed on a Setaram SENSYS Evo DSC calorimeter with a self-built U-shape sample tube. The fork-shape sample tube was connected to a Micromeritics 3Flex for the adsorption quantity measurement and temperature control as reported previously.[13] For each experiment used approximately 70 mg catalyst was loaded in the reactor. The gas pretreatment procedure was the same as mentioned above in a soak mode under 760 mmHg O_2. After pretreatment the catalyst was exposed to vacuum with pressure below $1e^{-5}$ mmHg. CO/O_2 adsorption experiment was measured at -75 °C with pressure between 0-300 mm Hg for O_2 calorimetry and 0–20 mmHg for CO calorimetry.

CO oxidation kinetic measurements. CO oxidation kinetic measurements were performed under differential conditions (<4% conversion) in a conventional laboratory tubular plug flow reactor (7 mm ID quartz tube). Dilution experiments were performed according to Koros-Nowak test to determine the necessary dilution ratio for measurements under strict kinetic control without mass and heat transfer

effects.[68-70] The catalysts (after intraparticle dilution) were pressed and sieved into a 106-250 μm diameter fraction. The dilution ratio test to eliminate transport limitations was performed on a more active 1% Pt/Al_2O_3 catalyst using SiO_2 as the diluent. Intraparticle dilutions ratio of 1:40, 1:200 and 1:1000 showed no difference in activity under different CO and O_2 conditions between 145 and 170 °C, which indicates the measured catalytic activity was evaluated under kinetic control without transport artifacts. 1:10 dilution ratio with SiO_2 was applied for the 1% Pt/CeO_2 single atom catalyst based on its activity. Each catalyst pretreatment was the same as mentioned above, and the total flow rate during pretreatment was kept at 50 sccm. The catalyst temperature was measured by a K-type thermocouple (OMEGA) attached at the center of the catalyst bed on the outside of the tube. After pretreatment, CO (5%, balance N_2, certified grade Airgas) was mixed with pure O_2 (99.999% Airgas) and He (99.999% Airgas, equipped with moisture/O_2 trap, Agilent OT3-2) at 35 °C to control the partial pressures of CO and O_2 (by varying their flowrates using Brooks mass flow controllers SLA5800 series). The CO gas line was equipped with a metal carbonyl purifier (Matheson, NanoChem Metal-X) to remove the trace amount of metal carbonyl and a molecular sieve 3A (8–12 mesh) trap to remove trace (ppm) levels of CO_2. No CO_2 was detected in the mass spectrometer with the CO or O_2 flowing during a blank test. The reactor was heated from room temperature to the reaction temperature at 3 °C/min in 0.5 kPa CO and 10 kPa O_2 balanced with He. During the steady state kinetic measurements, the conversion of CO was always below 4% by varying the total flow rate between 50-100 sccm. To investigate the effect of CO partial pressure on reaction rate, the partial pressure of O_2 was held constant at 10 kPa and the partial pressure of CO was varied between 0.3–1.0 kPa. To investigate the effect of O_2 partial pressure, the CO partial pressure was held constant at 1.0 kPa and the partial pressure of O_2 was varied between 2–14 kPa, then the measurements were repeated at the initial condition at 1 kPa CO partial pressure. We note that we rigorously monitored the catalyst stability by re-measuring the catalyst activity periodically

throughout the experiment under the first condition measured. The activity was stable (< 10% deactivation) for each catalyst tested during the entire kinetic measurement. The composition of the effluent gases was measured by a gas chromatograph (Inficon Micro GC Fusion with two modules each with a separate carrier gas, injector, column and thermal conductivity detector (TCD). Column A: Rt-Molsieve 5A, 0.25 mm ID (10m) using Ar as carrier gas. Column B: Rt-Q-Bond 0.25 mm ID (12m) using He as carrier gas. The reaction rates were normalized by the total moles of Pt, assuming that all Pt are on surface.

DFT calculations. All spin-polarized DFT calculations were performed in Vienna *Ab initio* Simulation Package (VASP)[71, 72] with the gradient-corrected PW91[73] exchange-correlation functional. The electronic wave functions were expanded in plane waves up to a cutoff energy of 400 eV and the ionic core electrons were approximated by the projector augmented-wave (PAW)[74] method. To describe properly the behavior of Ce *f* electrons, the DFT + *U* method[75, 76] with U = 4.5 eV was used. A low-energy CeO_2 monolayer-high step was selected as the slab model with the edge oriented along the $[1\bar{1}0]$ direction, containing nine atomic layers, which is consistent with the models of step II and step-U used in Ref. [77] and Ref. [78], respectively. The unit cell was about 7.65 ×13.25 Å^2, containing 20 Ce and 40 O atoms. In this model, Pt_1 adsorbed on the step and two excess oxygen atoms were added to obtain a stable square planar configuration of PtO_4. During the structural optimization, the bottom three atomic layers were fixed while the others as well as the adsorbates were fully relaxed. A vacuum space of 14 Å was employed to avoid the interaction between the neighboring interleaved slabs. To sample the Brillouin zone, a 2×1×1 Monkhorst-Pack[79] *k*-point grid was adopted, which was tested to be converged.

The adsorption energy of a pertinent species was calculated as follows: $E_{ads} = E_{(adsorbate + slab)} - E_{(adsorbate)} - E_{(slab)}$. The transition states (TSs) between initial states (ISs) and final states (FSs) were

determined using the climb image-nudged elastic band (CI-NEB) method.[80] The total energy difference was less than 10^{-4} eV and the convergence of relaxation was checked with a 0.05 eV/Å criterion.

ASSOCIATED CONTENT

Supporting Information

The Supporting Information is available free of charge on the ACS Publications website.

Supplementary figures and supplementary tables (PDF)

AUTHOR INFORMATION

Corresponding Author

* hguo@unm.edu; amkarim@vt.edu

Author Contributions

%: Y. L. and S. Z. contributed equally.

Notes

The authors declare no competing financial interest.

ACKNOWLEDGMENT

This research was primarily sponsored by the Army Research Office and was accomplished under Grant Numbers W911NF-16-1-0400 and W911NF-19-1-0308. CK and AMK also acknowledge support from the Army Research Office under Grant Number W911NF-20-2-0058. The views and conclusions contained in this document are those of the authors and should not be interpreted as representing the

official policies, either expressed or implied, of the Army Research Office or the U.S. Government. The U.S. Government is authorized to reproduce and distribute reprints for Government purposes notwithstanding any copyright notation herein. HG and AKD acknowledge the support from the Air Force Office of Scientific Research (Grant Number FA9550-18-1-0413). We also acknowledge NSF grant DMR-1828731 for acquisition of the AC-STEM. SZ thanks the support from the National Natural Science Foundation of China (Grant number 21962007), Jiangxi Provincial Natural Science Foundation (Grant number 2020BABL203009) and Foundation of Jiangxi Educational Committee (Grant number GJJ190697). SL thanks the National Natural Science Foundation of China (Grant numbers 21973013 and 21673040). Use of the Stanford Synchrotron Radiation Light Source (SSRL, beamline 9-3, user proposal 4645), SLAC National Accelerator Laboratory is supported by the U.S. Department of Energy, office of Basic Energy Sciences under Contract No. DE-AC02-76SF00515. Additional support by the Consortium for Operando and Advanced Catalyst Characterization via Electronic Spectroscopy and Structure (Co-ACCESS) at SLAC is acknowledged. Co-ACCESS, is supported by the U.S. Department of Energy, Office of Science, Office of Basic Energy Sciences, Chemical Sciences, Geosciences and Biosciences under Contract DE-AC02-76SF00515.

REFERENCES

1. Liu, L. C.; Corma, A., Metal Catalysts for Heterogeneous Catalysis: From Single Atoms to Nanoclusters and Nanoparticles. *Chem. Rev.* **2018,** *118* (10), 4981-5079.
2. Sun, S. H.; Zhang, G. X.; Gauquelin, N.; Chen, N.; Zhou, J. G.; Yang, S. L.; Chen, W. F.; Meng, X. B.; Geng, D. S.; Banis, M. N.; Li, R. Y.; Ye, S. Y.; Knights, S.; Botton, G. A.; Sham, T. K.; Sun, X. L., Single-atom Catalysis Using Pt/Graphene Achieved through Atomic Layer Deposition. *Scientific Reports* **2013,** *3*.
3. Wang, A. Q.; Li, J.; Zhang, T., Heterogeneous single-atom catalysis. *Nature Reviews Chemistry* **2018,** *2* (6), 65-81.
4. Ji, S.; Chen, Y.; Wang, X.; Zhang, Z.; Wang, D.; Li, Y., Chemical Synthesis of Single Atomic Site Catalysts. *Chem. Rev.* **2020**.

5. Qiao, B. T.; Wang, A. Q.; Yang, X. F.; Allard, L. F.; Jiang, Z.; Cui, Y. T.; Liu, J. Y.; Li, J.; Zhang, T., Single-atom catalysis of CO oxidation using Pt-1/FeOx. *Nat. Chem.* **2011,** *3* (8), 634-641.
6. Lin, J.; Wang, A. Q.; Qiao, B. T.; Liu, X. Y.; Yang, X. F.; Wang, X. D.; Liang, J. X.; Li, J. X.; Liu, J. Y.; Zhang, T., Remarkable Performance of Ir-1/FeOx Single-Atom Catalyst in Water Gas Shift Reaction. *Journal of the American Chemical Society* **2013,** *135* (41), 15314-15317.
7. Chen, Z. W.; Chen, L. X.; Yang, C. C.; Jiang, Q., Atomic (single, double, and triple atoms) catalysis: frontiers, opportunities, and challenges. *J. Mater. Chem. A* **2019,** *7* (8), 3492-3515.
8. Liu, J., Catalysis by Supported Single Metal Atoms. *ACS Catal.* **2017,** *7* (1), 34-59.
9. Fu, J.; Lym, J.; Zheng, W.; Alexopoulos, K.; Mironenko, A. V.; Li, N.; Boscoboinik, J. A.; Su, D.; Weber, R. T.; Vlachos, D. G., C–O bond activation using ultralow loading of noble metal catalysts on moderately reducible oxides. *Nat. Catal.* **2020**.
10. Lu, Y. B.; Wang, J. M.; Yu, L.; Kovarik, L.; Zhang, X. W.; Hoffman, A. S.; Gallo, A.; Bare, S. R.; Sokaras, D.; Kroll, T.; Dagle, V.; Xin, H. L.; Karim, A. M., Identification of the active complex for CO oxidation over single-atom Ir-on-MgAl2O4 catalysts. *Nat. Catal.* **2019,** *2* (2), 149-156.
11. Lu, Y.; Kuo, C.-T.; Kovarik, L.; Hoffman, A. S.; Boubnov, A.; Driscoll, D. M.; Morris, J. R.; Bare, S. R.; Karim, A. M., A versatile approach for quantification of surface site fractions using reaction kinetics: The case of CO oxidation on supported Ir single atoms and nanoparticles. *Journal of Catalysis* **2019,** *378*, 121-130.
12. Zhang, L. L.; Zhou, M. X.; Wang, A. Q.; Zhang, T., Selective Hydrogenation over Supported Metal Catalysts: From Nanoparticles to Single Atoms. *Chem. Rev.* **2020,** *120* (2), 683-733.
13. Kuo, C. T.; Lu, Y. B.; Kovarik, L.; Engelhard, M.; Karim, A. M., Structure Sensitivity of Acetylene Semi-Hydrogenation on Pt Single Atoms and Subnanometer Clusters. *ACS Catal.* **2019,** *9* (12), 11030-11041.
14. Yan, X.; Duan, P.; Zhang, F.; Li, H.; Zhang, H.; Zhao, M.; Zhang, X.; Xu, B.; Pennycook, S. J.; Guo, J., Stable single-atom platinum catalyst trapped in carbon onion graphitic shells for improved chemoselective hydrogenation of nitroarenes. *Carbon* **2019,** *143*, 378-384.
15. Yan, H.; Cheng, H.; Yi, H.; Lin, Y.; Yao, T.; Wang, C.; Li, J.; Wei, S.; Lu, J., Single-Atom Pd/Graphene Catalyst Achieved by Atomic Layer Deposition: Remarkable Performance in Selective Hydrogenation of 1,3-Butadiene. *J. Am. Chem. Soc.* **2015**.
16. Lin, L.; Yao, S.; Gao, R.; Liang, X.; Yu, Q.; Deng, Y.; Liu, J.; Peng, M.; Jiang, Z.; Li, S.; Li, Y. W.; Wen, X. D.; Zhou, W.; Ma, D., A highly CO-tolerant atomically dispersed Pt catalyst for chemoselective hydrogenation. *Nat Nanotechnol* **2019,** *14* (4), 354-361.
17. Shan, J.; Li, M.; Allard, L. F.; Lee, S.; Flytzani-Stephanopoulos, M., Mild oxidation of methane to methanol or acetic acid on supported isolated rhodium catalysts. *Nature* **2017,** *551* (7682), 605-608.
18. Matsubu, J. C.; Yang, V. N.; Christopher, P., Isolated metal active site concentration and stability controls catalytic CO2 reduction selectivity. *J. Am. Chem. Soc.* **2015**.
19. Herzing, A. A.; Kiely, C. J.; Carley, A. F.; Landon, P.; Hutchings, G. J., Identification of active gold nanoclusters on iron oxide supports for CO oxidation. *Science* **2008,** *321* (5894), 1331-1335.

20. Cui, X.; Li, W.; Ryabchuk, P.; Junge, K.; Beller, M., Bridging homogeneous and heterogeneous catalysis by heterogeneous single-metal-site catalysts. *Nat. Catal.* **2018,** *1* (6), 385-397.
21. Tang, Y.; Li, Y. T.; Fung, V.; Jiang, D. E.; Huang, W. X.; Zhang, S. R.; Iwasawa, Y.; Sakata, T.; Nguyen, L.; Zhang, X. Y.; Frenkel, A. I.; Tao, F., Single rhodium atoms anchored in micropores for efficient transformation of methane under mild conditions. *Nat. Commun.* **2018,** *9*.
22. Chen, Y. X.; Huang, Z. W.; Ma, Z.; Chen, J. M.; Tang, X. F., Fabrication, characterization, and stability of supported single-atom catalysts. *Catal. Sci. Technol.* **2017,** *7* (19), 4250-4258.
23. Chen, Y. J.; Ji, S. F.; Chen, C.; Peng, Q.; Wang, D. S.; Li, Y. D., Single-Atom Catalysts: Synthetic Strategies and Electrochemical Applications. *Joule* **2018,** *2* (7), 1242-1264.
24. Kunwar, D.; Zhou, S.; De La Riva, A.; Peterson, E.; Xiong, H.; Pereira Hernandez, X. I.; Purdy, S. C.; ter Veen, R.; Brongersma, H. H.; Miller, J. T.; Hashiguchi, H.; Kovarik, L.; Lin, S.; Guo, H.; Wang, Y.; Datye, A., Stabilizing High Metal Loadings of Thermally Stable Platinum Single Atoms on an Industrial Catalyst Support. *ACS Catal.* **2019**.
25. Jones, J.; Xiong, H. F.; Delariva, A. T.; Peterson, E. J.; Pham, H.; Challa, S. R.; Qi, G. S.; Oh, S.; Wiebenga, M. H.; Hernandez, X. I. P.; Wang, Y.; Datye, A. K., Thermally stable single-atom platinum-on-ceria catalysts via atom trapping. *Science* **2016,** *353* (6295), 150-154.
26. Zhang, Z.; Zhu, Y.; Asakura, H.; Zhang, B.; Zhang, J.; Zhou, M.; Han, Y.; Tanaka, T.; Wang, A.; Zhang, T.; Yan, N., Thermally stable single atom Pt/m-Al2O3 for selective hydrogenation and CO oxidation. *Nat Commun* **2017,** *8*, 16100.
27. Wang, Y.; Yuan, H.; Li, Y.; Chen, Z., Two-dimensional iron-phthalocyanine (Fe-Pc) monolayer as a promising single-atom-catalyst for oxygen reduction reaction: a computational study. *Nanoscale* **2015,** *7* (27), 11633-41.
28. Kistler, J. D.; Chotigkrai, N.; Xu, P.; Enderle, B.; Praserthdam, P.; Chen, C. Y.; Browning, N. D.; Gates, B. C., A single-site platinum CO oxidation catalyst in zeolite KLTL: microscopic and spectroscopic determination of the locations of the platinum atoms. *Angew. Chem. Int. Ed. Engl.* **2014,** *53* (34), 8904-7.
29. Yang, M.; Li, S.; Wang, Y.; Herron, J. A.; Xu, Y.; Allard, L. F.; Lee, S.; Huang, J.; Mavrikakis, M.; Flytzani-Stephanopoulos, M., Catalytically active Au-O(OH)(x)-species stabilized by alkali ions on zeolites and mesoporous oxides. *Science* **2014,** *346* (6216), 1498-1501.
30. DeRita, L.; Resasco, J.; Dai, S.; Boubnov, A.; Thang, H. V.; Hoffman, A. S.; Ro, I.; Graham, G. W.; Bare, S. R.; Pacchioni, G.; Pan, X.; Christopher, P., Structural evolution of atomically dispersed Pt catalysts dictates reactivity. *Nat Mater* **2019,** *18* (7), 746-751.
31. Nie, L.; Mei, D. H.; Xiong, H. F.; Peng, B.; Ken, Z. B.; Hernandez, X. I. P.; DeLariva, A.; Wang, M.; Engelhard, M. H.; Kovarik, L.; Datye, A. K.; Wang, Y., Activation of surface lattice oxygen in single-atom Pt/Ce0(2) for low-temperature CO oxidation. *Science* **2017,** *358* (6369), 1419-+.
32. Therrien, A. J.; Hensley, A. J. R.; Marcinkowski, M. D.; Zhang, R. Q.; Lucci, F. R.; Coughlin, B.; Schilling, A. C.; McEwen, J. S.; Sykes, E. C. H., An atomic-scale view of single-site Pt catalysis for low-temperature CO oxidation. *Nat. Catal.* **2018,** *1* (3), 192-198.

33. Yang, M.; Liu, J.; Lee, S.; Zugic, B.; Huang, J.; Allard, L. F.; Flytzani-Stephanopoulos, M., A Common Single-Site Pt(II)-O(OH)x- Species Stabilized by Sodium on "Active" and "Inert" Supports Catalyzes the Water-Gas Shift Reaction. *J. Am. Chem. Soc.* **2015,** *137* (10), 3470-3.

34. Cao, L.; Liu, W.; Luo, Q.; Yin, R.; Wang, B.; Weissenrieder, J.; Soldemo, M.; Yan, H.; Lin, Y.; Sun, Z.; Ma, C.; Zhang, W.; Chen, S.; Wang, H.; Guan, Q.; Yao, T.; Wei, S.; Yang, J.; Lu, J., Atomically dispersed iron hydroxide anchored on Pt for preferential oxidation of CO in H2. *Nature* **2019,** *565* (7741), 631-635.

35. Li, Z.; Ji, S. F.; Liu, Y. W.; Cao, X.; Tian, S. B.; Chen, Y. J.; Niu, Z. G.; Li, Y. D., Well-Defined Materials for Heterogeneous Catalysis: From Nanoparticles to Isolated Single-Atom Sites. *Chem. Rev.* **2020,** *120* (2), 623-682.

36. Maurer, F.; Jelic, J.; Wang, J.; Gänzler, A.; Dolcet, P.; Wöll, C.; Wang, Y.; Studt, F.; Casapu, M.; Grunwaldt, J.-D., Tracking the formation, fate and consequence for catalytic activity of Pt single sites on CeO2. *Nat. Catal.* **2020**.

37. Montini, T.; Melchionna, M.; Monai, M.; Fornasiero, P., Fundamentals and Catalytic Applications of CeO2-Based Materials. *Chem. Rev.* **2016,** *116* (10), 5987-6041.

38. Nagai, Y.; Dohmae, K.; Ikeda, Y.; Takagi, N.; Tanabe, T.; Hara, N.; Guilera, G.; Pascarelli, S.; Newton, M. A.; Kuno, O.; Jiang, H. Y.; Shinjoh, H.; Matsumoto, S., In Situ Redispersion of Platinum Autoexhaust Catalysts: An On-Line Approach to Increasing Catalyst Lifetimes? *Angew. Chem. Int. Ed.* **2008,** *47* (48), 9303-9306.

39. Kottwitz, M.; Li, Y.; Palomino, R. M.; Liu, Z.; Wang, G.; Wu, Q.; Huang, J.; Timoshenko, J.; Senanayake, S. D.; Balasubramanian, M.; Lu, D.; Nuzzo, R. G.; Frenkel, A. I., Local Structure and Electronic State of Atomically Dispersed Pt Supported on Nanosized CeO2. *ACS Catal.* **2019**.

40. Resasco, J.; DeRita, L.; Dai, S.; Chada, J. P.; Xu, M. J.; Yan, X. X.; Finzel, J.; Hanukovich, S.; Hoffman, A. S.; Graham, G. W.; Bare, S. R.; Pan, X. Q.; Christopher, P., Uniformity Is Key in Defining Structure-Function Relationships for Atomically Dispersed Metal Catalysts: The Case of Pt/CeO2. *Journal of the American Chemical Society* **2020,** *142* (1), 169-184.

41. Tang, Y.; Wang, Y.-G.; Li, J., Theoretical Investigations of Pt1@CeO2 Single-Atom Catalyst for CO Oxidation. *The Journal of Physical Chemistry C* **2017,** *121* (21), 11281-11289.

42. Lu, Y. B.; Thompson, C.; Kunwar, D.; Datye, A. K.; Karim, A. M., Origin of the High CO Oxidation Activity on CeO2 Supported Pt Nanoparticles: Weaker Binding of CO or Facile Oxygen Transfer from the Support? *Chemcatchem* **2020,** *12* (6), 1726-1733.

43. Ferre, G.; Aouine, M.; Bosselet, F.; Burel, L.; Aires, F. J. C. S.; Geantet, C.; Ntais, S.; Maurer, F.; Casapu, M.; Grunwaldt, J. D.; Epicier, T.; Loridant, S.; Vernoux, P., Exploiting the dynamic properties of Pt on ceria for low-temperature CO oxidation. *Catal. Sci. Technol.* **2020,** *10* (12), 3904-3917.

44. Xiao, Y. C.; Li, H.; Xie, K., Activating Lattice Oxygen at the Twisted Surface in a Mesoporous CeO2 Single Crystal for Efficient and Durable Catalytic CO Oxidation. *Angew. Chem. Int. Ed.* **2021,** *60* (10), 5240-5244.

45. Feng, Y.; Wan, Q.; Xiong, H.; Zhou, S.; Chen, X.; Pereira Hernandez, X. I.; Wang, Y.; Lin, S.; Datye, A. K.; Guo, H., Correlating DFT Calculations with CO Oxidation Reactivity on Ga-Doped Pt/CeO2 Single-Atom Catalysts. *The Journal of Physical Chemistry C* **2018,** *122* (39), 22460-22468.

46. Ganzler, A. M.; Casapu, M.; Vernoux, P.; Loridant, S.; Aires, F. J. C. S.; Epicier, T.; Betz, B.; Hoyer, R.; Grunwaldt, J. D., Tuning the Structure of Platinum Particles on Ceria InSitu for Enhancing the Catalytic Performance of Exhaust Gas Catalysts. *Angew. Chem. Int. Ed.* **2017,** *56* (42), 13078-13082.
47. Ganzler, A. M.; Casapu, M.; Maurer, F.; Stormer, H.; Gerthsen, D.; Ferre, G.; Vernaux, P.; Bornmann, B.; Frahm, R.; Murzin, V.; Nachtegaal, M.; Votsmeier, M.; Grunwaldt, J. D., Tuning the Pt/CeO2 Interface by in Situ Variation of the Pt Particle Size. *ACS Catal.* **2018,** *8* (6), 4800-4811.
48. Gänzler, A. M.; Casapu, M.; Doronkin, D. E.; Maurer, F.; Lott, P.; Glatzel, P.; Votsmeier, M.; Deutschmann, O.; Grunwaldt, J.-D., Unravelling the Different Reaction Pathways for Low Temperature CO Oxidation on Pt/CeO2 and Pt/Al2O3 by Spatially Resolved Structure–Activity Correlations. *The Journal of Physical Chemistry Letters* **2019,** *10* (24), 7698-7705.
49. An, K.; Alayoglu, S.; Musselwhite, N.; Plamthottam, S.; Melaet, G.; Lindeman, A. E.; Somorjai, G. A., Enhanced CO Oxidation Rates at the Interface of Mesoporous Oxides and Pt Nanoparticles. *Journal of the American Chemical Society* **2013,** *135* (44), 16689-16696.
50. Bunluesin, T.; Gorte, R. J.; Graham, G. W., CO oxidation for the characterization of reducibility in oxygen storage components of three-way automotive catalysts. *Appl. Catal. B: Environ.* **1997,** *14* (1), 105-115.
51. Bunluesin, T.; Gorte, R. J.; Graham, G. W., Studies of the water-gas-shift reaction on ceria-supported Pt, Pd, and Rh: Implications for oxygen-storage properties. *Appl. Catal. B: Environ.* **1998,** *15* (1), 107-114.
52. Pereira-Hernandez, X. I.; DeLaRiva, A.; Muravev, V.; Kunwar, D.; Xiong, H.; Sudduth, B.; Engelhard, M.; Kovarik, L.; Hensen, E. J. M.; Wang, Y.; Datye, A. K., Tuning Pt-CeO2 interactions by high-temperature vapor-phase synthesis for improved reducibility of lattice oxygen. *Nat Commun* **2019,** *10* (1), 1358.
53. Xia, Z.; Zhang, H.; Shen, K.; Qu, Y.; Jiang, Z., Wavelet analysis of extended X-ray absorption fine structure data: Theory, application. *Physica B: Condensed Matter* **2018,** *542*, 12-19.
54. Timoshenko, J.; Kuzmin, A., Wavelet data analysis of EXAFS spectra. *Comput. Phys. Commun.* **2009,** *180* (6), 920-925.
55. Ding, K.; Gulec, A.; Johnson, A. M.; Schweitzer, N. M.; Stucky, G. D.; Marks, L. D.; Stair, P. C., Identification of active sites in CO oxidation and water-gas shift over supported Pt catalysts. *Science* **2015,** *350* (6257), 189-192.
56. Alexopoulos, K.; Wang, Y. F.; Vlachos, D. G., First-Principles Kinetic and Spectroscopic Insights into Single-Atom Catalysis. *ACS Catal.* **2019,** *9* (6), 5002-5010.
57. Sravan Kumar, K. B.; Deshpande, P. A., On Identification of Labile Oxygen in Ceria-Based Solid Solutions: Which Oxygen Leaves the Lattice? *The Journal of Physical Chemistry C* **2015,** *119* (16), 8692-8702.
58. Migani, A.; Vayssilov, G. N.; Bromley, S. T.; Illas, F.; Neyman, K. M., Greatly facilitated oxygen vacancy formation in ceria nanocrystallites. *Chem. Commun.* **2010,** *46* (32), 5936-5938.
59. Di Benedetto, A.; Landi, G.; Lisi, L., CO reactive adsorption at low temperature over CuO/CeO2 structured catalytic monolith. *Int. J. Hydrogen Energy* **2017,** *42* (17), 12262-12275.
60. Yoo, M.; Yu, Y. S.; Ha, H.; Lee, S.; Choi, J. S.; Oh, S.; Kang, E.; Choi, H.; An, H.; Lee, K. S.; Park, J. Y.; Celestre, R.; Marcus, M. A.; Nowrouzi, K.; Taube, D.; Shapiro, D. A.; Jung,

W.; Kim, C.; Kim, H. Y., A tailored oxide interface creates dense Pt single-atom catalysts with high catalytic activity. *Energy & Environmental Science* **2020,** *13* (4), 1231-1239.

61. Daelman, N.; Capdevila-Cortada, M.; Lopez, N., Dynamic charge and oxidation state of Pt/CeO2 single-atom catalysts. *Nat. Mater.* **2019,** *18* (11), 1215-+.
62. Karim, A. M.; Howard, C.; Roberts, B.; Kovarik, L.; Zhang, L.; King, D. L.; Wang, Y., In Situ X-ray Absorption Fine Structure Studies on the Effect of pH on Pt Electronic Density during Aqueous Phase Reforming of Glycerol. *ACS Catal.* **2012,** *2* (11), 2387-2394.
63. Ravel, B.; Newville, M., ATHENA, ARTEMIS, HEPHAESTUS: data analysis for X-ray absorption spectroscopy using IFEFFIT. *Journal of Synchrotron Radiation* **2005,** *12*, 537-541.
64. Newville, M., IFEFFIT: interactive XAFS analysis and FEFF fitting. *Journal of Synchrotron Radiation* **2001,** *8*, 322-324.
65. Zabinsky, S. I.; Rehr, J. J.; Ankudinov, A.; Albers, R. C.; Eller, M. J., Multiple-scattering calculations of x-ray-absorption spectra. *Physical Review B* **1995,** *52* (4), 2995-3009.
66. Muñoz, M.; Argoul, P.; Farges, F. o., Continuous Cauchy wavelet transform analyses of EXAFS spectra: A qualitative approach. *Am. Mineral.* **2003,** *88* (4), 694-700.
67. Newville, M., Larch: An Analysis Package for XAFS and Related Spectroscopies. *Journal of Physics: Conference Series* **2013,** *430*, 012007.
68. Bonet, F.; Grugeon, S.; Dupont, L.; Urbina, R. H.; Boudart, M.; Djega-Mariadassou, G., *Kinetics of Heterogeneous Catlytic Reactions*. Princeton University Press / Princeton, N.J.: 1984.
69. Koros, R. M.; Nowak, E. J., A diagnostic test of the kinetic regime in a packed bed reactor. *Chem. Eng. Sci.* **1967,** *22* (3), 470.
70. Madon, R. J.; Boudart, M., Experimental criterion for the absence of artifacts in the measurement of rates of heterogeneous catalytic reactions. *Industrial & Engineering Chemistry Fundamentals* **1982,** *21* (4), 438-447.
71. Kresse, G.; Furthmuller, J., Efficient iterative schemes for ab initio total-energy calculations using a plane-wave basis set. *Physical Review B* **1996,** *54* (16), 11169-11186.
72. Kresse, G.; Furthmuller, J., Efficiency of ab-initio total energy calculations for metals and semiconductors using a plane-wave basis set. *Computational Materials Science* **1996,** *6* (1), 15-50.
73. Perdew, J. P.; Chevary, J. A.; Vosko, S. H.; Jackson, K. A.; Pederson, M. R.; Singh, D. J.; Fiolhais, C., Atoms, molecules, solids, and surfaces: Applications of the generalized gradient approximation for exchange and correlation. *Physical Review B* **1992,** *46* (11), 6671-6687.
74. Blochl, P. E., Projector Augmented-Wave Method. *Physical Review B* **1994,** *50* (24), 17953-17979.
75. Krcha, M. D.; Janik, M. J., Challenges in the use of density functional theory to examine catalysis by M-doped ceria surfaces. *International Journal of Quantum Chemistry* **2014,** *114* (1), 8-13.
76. McFarland, E. W.; Metiu, H., Catalysis by Doped Oxides. *Chem. Rev.* **2013,** *113* (6), 4391-4427.
77. Dvořák, F.; Camellone, M. F.; Tovt, A.; Tran, N.-D.; Negreiros, F. R.; Vorokhta, M.; Skála, T.; Matolínová, I.; Mysliveček, J.; Matolín, V., Creating single-atom Pt-ceria catalysts by surface step decoration. *Nat. Commun.* **2016,** *7*.

78. Liu, J.-C.; Wang, Y.-G.; Li, J., Toward Rational Design of Oxide-Supported Single-Atom Catalysts: Atomic Dispersion of Gold on Ceria. *Journal of the American Chemical Society* **2017,** *139* (17), 6190-6199.

79. Monkhorst, H. J.; Pack, J. D., Special points for Brillouin-zone integrations. *Physical Review B* **1976,** *13* (12), 5188-5192.

80. Henkelman, G.; Uberuaga, B. P.; Jónsson, H., A climbing image nudged elastic band method for finding saddle points and minimum energy paths. *The Journal of Chemical Physics* **2000,** *113* (22), 9901-9904.

Manuscript published in ACS Catal. 2021, 11, 8701−8715
https://doi.org/10.1021/acscatal.1c01900

Table of Contents artwork